Preprint

The 2025 M_w 7.1 Tingri (South Tibet) Earthquake: Rupture of Normal Conjugate Optimally Oriented Faults, Shallow Coseismic Slip Deficit, and Early Afterslip

Authors: Xiaoyu Zou and Yuri Fialko

Institute of Geophysics and Planetary Physics, Scripps Institution of Oceanography, University of California San Diego

9500 Gilman Dr., La Jolla, CA 92093-0225

manuscript accepted for publication in Seismological Research Letters

The 2025 M_w 7.1 Tingri (South Tibet) Earthquake: Rupture of Normal Conjugate Optimally Oriented Faults, Shallow Coseismic Slip Deficit, and Early Afterslip

Xiaoyu Zou[*1] and Yuri Fialko[1]

Abstract

On 7 January 2025, a magnitude 7.1 earthquake struck Tingri County at the south of the Tibetan Plateau, China, producing widespread damage in the Lhatse-Sa'gya-Tingri region and adjacent areas. The earthquake ruptured a pair of conjugate north-south striking normal faults in the Dengmecuo graben, and was the largest normal earthquake instrumentally recorded in the region. We use Interferometric Synthetic Aperture (InSAR) observations from Sentinel-1A, ALOS-2, and Lutan-1 satellites to investigate coseismic and early postseismic deformation due to the 2025 Tingri earthquake. We invert line of sight (LOS) displacements and pixel offsets for the fault geometry and slip distribution using an iterative scheme that incorporates a 3-D curved fault geometry and layered rigidity structure constrained by seismic tomography. The ruptured faults are modeled using a triangular mesh with a linear variation in slip between the nodes. The preferred model suggests average dip angles of 60-70° for both the main (west-dipping) rupture, and the subsidiary (east-dipping) conjugate fault, indicating optimal fault orientations consistent with Byerlee's law and coefficient of friction of 0.6-0.7. The best-fit model has a variance reduction of 91%, and an equivalent moment magnitude of 7.0. The modeled coseismic slip exhibits a large (∼60%) shallow slip deficit, only a small fraction of which is relieved by shallow afterslip in the first ∼8 months following the earthquake. The observed coseismic and postseismic deformation suggest velocity-strengthening friction, as well as extensive off-fault damage in the top several kilometers of the Earth's crust. Contributions from the early viscoelastic and poroelastic relaxation are found to be negligible. Continued geodetic observations will help quantify the evolving roles of afterslip and viscoelastic relaxation, provide tighter constraints on the effective rheology of the lower crust, and illuminate the mechanisms of the ongoing E–W extension in the Southern Tibetan Rift Zone.

Cite this article as Xiaoyu Zou, Yuri Fialko (2022). The 2025 M_w 7.1 Tingri (South Tibet) Earthquake: Rupture of Normal Conjugate Optimally Oriented Faults, Shallow Coseismic Slip Deficit, and Early Afterslip, *Seismol. Res. Lett.* **XX**, 1–15, doi: 00.0000/000000000.

Supplemental Material

Introduction

On January 7th, 2025 at 01:05 UTC time, the moment magnitude (M_w) 7.1 earthquake struck Tingri County of the Tibet Autonomous Region, China, with an epicenter located at [28.604°N, 87.378°E] and a focal depth of 10 km (USGS 2025). The earthquake is the largest instrumentally recorded normal event in the Southern Tibetan Plateau, and the most destructive one since the 2015 M_w 7.8 Gorkha (Nepal) earthquake (e.g. Hall et al. 2017; Wang and Fialko 2018; Qi et al. 2024). With an estimated intensity of IX, the 2025 Tingri (also referred to as Dingri) earthquake has devastated the Lhatse-Sa'gya-Tingri region, killing at least 126 people and destroying more than 3600 houses (e.g. Zhou and Li 2025). The impact extended beyond China, with Bhutan, India, and Nepal also reporting casualties and property damage. Early reports using the GCMT focal mechanism, satellite remote sensing data, and field observations showed that the earthquake ruptured a preexisting north-south trending westward-dipping normal fault, the Dengmecuo fault (DMCF; e.g. Zhou and Li 2025; Kusky and Meng 2025; Yu et al. 2025). The DMCF is aligned with other major normal faults in the rift system of southern

1. Institute of Geophysics and Planetary Physics, Scripps Institution of Oceanography, University of California San Diego, La Jolla, CA 92093, USA.
*Corresponding author: x3zou@ucsd.edu

Tibet, including the nearby Shenzha-Dingjie Fault System (Fig. 1). Several mechanisms have been proposed to drive the east–west extension of the Southern Tibet Rift System, including the gravitational spreading due to crustal thickening of the Tibetan Plateau (e.g. Molnar et al. 1993; Yang et al. 2025), oblique convergence between the Eurasian and Indian plates (e.g. McCaffrey and Nabelek 1998), and asthenospheric upwelling beneath the Eurasian plate (e.g. Pang et al. 2018; Qiao et al. 2025). Active extension within the Southern Tibetan Rift implies a considerable seismic hazard. Estimates of the slip rate deficit based on Global Navigational Satellite System (GNSS) measurements suggested that normal faults in the region have the potential to generate earthquakes with magnitude 7 or greater (Li et al. 2025).

As the Dengmecuo fault was not associated with any notable seismic activity prior to the 2025 Tingri earthquake, its size, geometry, and slip history were largely unknown. Initial studies of the Tingri earthquake using seismic and Interferometric Synthetic Aperture Radar (InSAR) data revealed a predominantly normal slip on a ∼50 km-long westward-dipping fault (e.g. Yu et al. 2025; Liu et al. 2025; Qiao et al. 2025; Yang et al. 2025; Chong et al. 2025). However, the reported dip angles vary considerably, from 41° (Yu et al. 2025) to 49° (USGS 2025) to 71° (Zhu et al. 2025), possibly due to a limited resolving power and/or coverage of various data sets, inversion algorithms, or over-simplified model assumptions. Robust constraints on the orientation of active faults are of considerable interest as they can be used to constrain in situ fault strength (e.g. Collettini and Sibson 2001; Fialko 2021; Zou et al. 2023; Scholz 2019, p. 107). Most of the previous studies of the 2025 Tingri earthquake approximated the earthquake rupture as a planar fault in a homogeneous elastic half-space (e.g. Yu et al. 2025; Liu et al. 2025). Another major limitation was the lack of the near-field data due to a strong decorrelation of the radar phase in Sentinel-1A (C-band) interferograms (e.g., Yu et al. 2025; Qiao et al. 2025). In this study, we combine interferometric phase measurements from Sentinel-1A satellite with those from the L-band ALOS-2 and Lutan-1 (LT-1) satellites, as well as with pixel offset data to provide a full coverage of coseismic displacements from different lines of sight (LOS). We use these data to map the rupture trace, and invert for the non-planar subsurface fault geometry and slip distribution (e.g., Simons et al. 2002; Furuya and Yasuda 2011; Dutta et al. 2021). Our coseismic slip models use Green's functions for a layered elastic half-space consistent with the local seismic velocity structure (e.g., Huang et al. 2020; Tan et al. 2023). We also include in our models a conjugate east-dipping fault to the west of the main rupture that was omitted in many previous studies. Finally, we present InSAR measurements of postseismic deformation that occurred during the first 8 months following the 2025 Tingri earthquake. A joint consideration of coseismic and postseismic deformation helps further reduce uncertainties in the rupture geometry and frictional properties of the host rocks (e.g., Lindsey and Fialko 2016; Jin et al. 2022).

Data and Methods

Analysis of Satellite Data

We use Synthetic Aperture Radar (SAR) data from Sentinel-1A (C-band, ascending track 12, descending track 48, and descending track 121), ALOS-2 (L-band, descending track 165, frame 3040), and LT-1 (L-band, ascending track 70) satellites. The spatial coverage, timespans, and perpendicular baselines of all input data are shown in Fig. 1, and Figs. S1–S3, and Tables S1 and S2 in the Supplementary Materials. The Sentinel-1A and ALOS-2 data are processed using GMTSAR (Sandwell et al. 2011). We remove the topographic phase using a digital elevation model from the Shuttle Radar Topography Mission (Farr et al. 2007). The residual phase is filtered using a Gaussian filter with a wavelength of 300 m, and unwrapped using the residue-cut algorithm (Goldstein and Werner 1998). Since the near-field radar phase in C-band is heavily decorrelated due to high displacement gradients and surface disruption, we compute pixel offsets for Sentinel-1A ascending track 12 and descending track 121, and ALOS-2 descending track 165. The pixel offset maps are quality checked and obvious outliers and noisy areas are masked out. We only use the range offsets, as the azimuth offsets have a low signal-to-noise ratio. The unwrapped radar phase from the LT-1 satellite is from a study by Yang et al. (2025).

We subsequently use Sentinel-1A range offsets and ALOS-2 and LT-1 interferograms to map the surface rupture. The data clearly show displacement discontinuities along two sub-parallel north-south trending faults, a ∼50-km long rupture near the 87.5° longitude ("main fault"), and a smaller rupture about 20 km to the west ("sub-fault"), see Figs. 1 and S1-S2. We obtain rupture traces for both the main fault and the sub-fault by digitizing the respective displacement discontinuities, see black dashed lines in Figs. 1 and S1-S2.

Coseismic interferograms and pixel offsets may contain "ramps" due to long-wavelength variations in the troposphere, ionosphere, and/or imprecise orbit data or timing errors (e.g. Wang and Jónsson 2014; Zhang et al. 2019). We correct for such artifacts using an iterative procedure. First, we subtract the best-fit planar ramp from the original data. We then carry out a linear inversion of down-sampled data for the assumed initial fault geometry discretized using triangular dislocation elements (TDE) in a homogeneous elastic half-space (Nikkhoo and Walter 2015). We subtract model predictions from the data and use residuals to estimate the best-fit quadratic surface. The latter is subsequently subtracted from the data, and iterations continue. After the initial iteration, we down-sample the data using

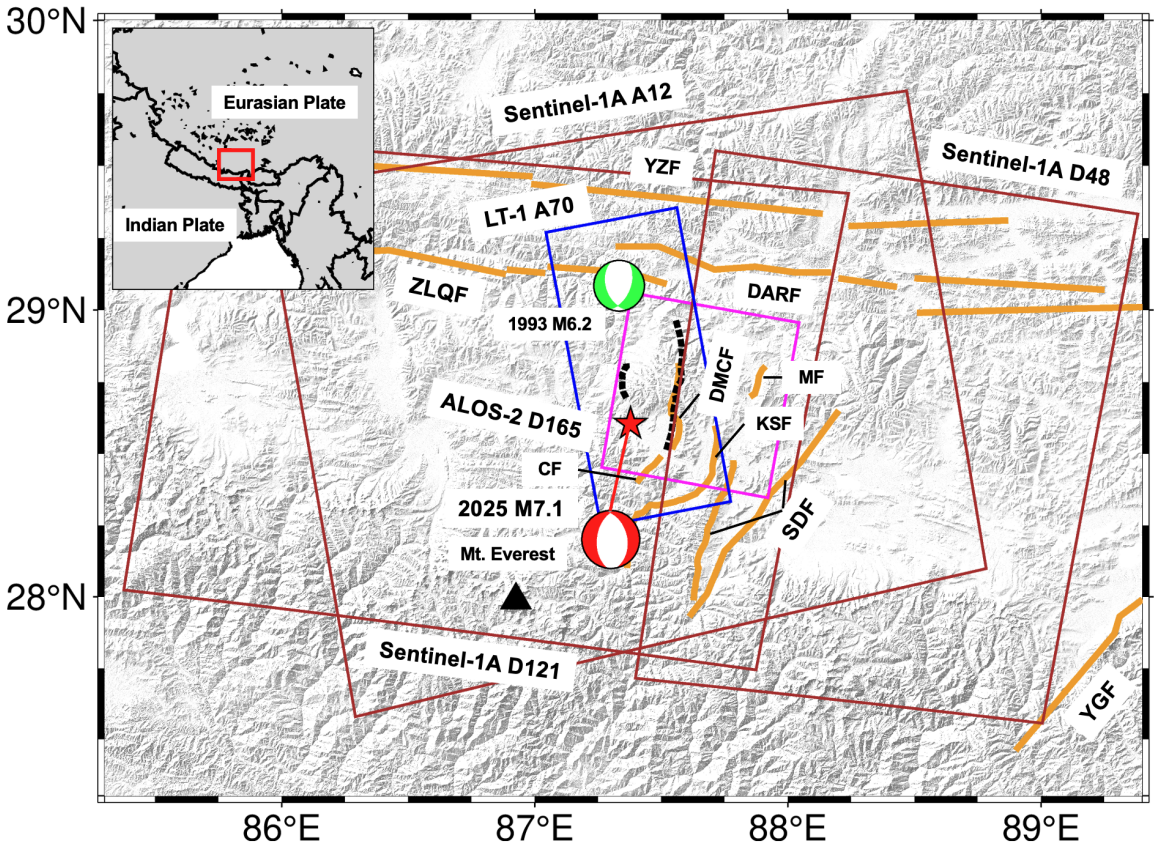

Figure 1. Regional map of the 2025 Tingri earthquake. The colored boxes denote the coverage area of the InSAR data used in our study. Brown boxes: Sentinel-1A; Magenta box: ALOS-2; Blue box: LT-1. The black dashed lines represent the fault traces of the main fault and the sub-fault. The red star is the earthquake epicenter of the Tingri earthquake, and the red beachball represents its focal mechanism. The green beachball represents the 1993 M_w 6.2 earthquake. The black triangle denotes location of Mount Everest. The black solid lines are mapped traces of major faults in the region, and the black dashed lines represent the seismogenic faults of the 2025 event (Wu et al. 2024; Liu et al. 2025). DMCF: Dengmecuo Fault; SDF: Shenzha-Dingjie fault; ZLQF: Zada-Lazi-Qiongdojiang fault; DARF: Dajiling-Angren-Renbu fault; YZF: Yarlung Zangbo fault.

Alt-text: Shaded-relief map of south Tibet showing the 2025 Mw 7.1 Tingri earthquake region. Colored rectangles outline InSAR scene footprints (Sentinel-1A ascending A12 and descending D48/D121; ALOS-2 D165; Lutan-1 A70). Thick black solid lines mark major mapped faults, and black dashed lines trace the modeled main and sub-faults. A red star marks the epicenter; a red focal-mechanism beachball indicates the 2025 event; a green beachball marks the 1993 Mw 6.2 earthquake. A black triangle indicates Mt. Everest. An inset map shows the location near the India–Eurasia plate boundary.

the gradient-based quad-tree algorithm and the current best-fit model to avoid over-sampling of a high-frequency noise (Wang and Fialko 2015) . Before de-trending the residuals, we mask out the near-field data (~ 20 km on each side of the main fault trace) to minimize the influence of potential model-related errors. The de-ramping procedure typically converges after 2-3 iterations.

Inversions for Fault Geometry and Slip Distribution

The de-trended line of sight (LOS) displacements and range offsets are used in joint inversions to estimate the subsurface fault geometry and slip distribution. We approximate each fault using a smooth curved surface that honors the fault trace. At the down-dip end, the surface follows a straight line that parallels the surface trace, but is offset horizontally according to the assumed dip angle. The curved surface is smoothly varying to satisfy both the top and bottom constraints on the rupture geometry. Based on the wavelength of the observed coseismic displacements and a few trial inversions, the main fault and the sub-fault are assumed to extend to depths of 25 and 7 km, respectively. The resulting curved fault surfaces are tessellated into a mesh consisting of triangular elements of variable size (see Supplementary Materials for details). The element size increases with depth

to account for the depth-dependent model resolution (e.g. Fialko 2004).

We use an improved and more realistic parameterization of fault slip that allows for linear (rather than piece-wise constant) variations in slip between the mesh nodes (vertices of triangular elements). Given a triangular mesh representing the best-fit fault geometry (Fig. 2), we compute composite Green's functions for each node of the mesh using a superposition of point sources for all triangles that share the respective vertex (see Supplementary Text S1 and Fig. S7). Green's functions for individual point sources (Wang et al. 2006) are computed for a layered rigidity structure (Fig. S4) derived from the 3-D shear-wave (Vs) velocity model (Huang et al. 2020). The elastic moduli are found using the empirical relationship between the body wave velocities and density (Brocher 2005). We solve for the slip distribution u at the mesh vertices by minimizing the following functional,

$$F(u,\lambda) = ||Gu - d||_2 + \lambda||\nabla^2 u||_2, \quad (1)$$

where G is the matrix of composite Green's functions, d is the data vector, u is the unknown slip distribution at the nodes (including strike- and dip-slip components), $||\cdot||_2$ is the L_2 norm, ∇^2 is a Laplacian operator, and λ is a smoothing parameter (Golub et al. 1999) chosen based on the trade-off curve between the model roughness and data misfit (see SI Text S1, Figs. S5–S7 for details). Because changes in radar range have limited sensitivity to meridional (north-south) displacements, the strike-slip component is less constrained compared to the dip-slip component. To suppress potential artifacts, we apply a stronger (by a factor of 3) smoothing to strike-slip compared to dip-slip.

We perform a grid search to find the best-fit dip angles of the two faults. To regularize the inversion, we first perform a grid search for the main fault alone. We vary the dip angle from 30° to 75° in 5° increments. For each assumed dip angle, we calculate the Green's functions for a new fault geometry and layered half-space and perform a least-squares linear inversion. We identify the best-fit dip angle based on the RMS of the residuals of all trial inversions. We then subtract the modeled contribution of the main fault from the data and invert the residuals for the best-fit dip angle of the sub-fault. The latter grid search is performed for a wider range of dip angles, 30-150° (i.e, allowing for both eastward and westward dip), given no prior information on the attitude of the sub-fault. Only the datasets with sufficient coverage around the sub-fault are used in the respective grid search. Next, we use the inferred best-fit geometries to resample the data based on the model. The modeled contribution of the sub-fault is subtracted from the data, and the procedure is repeated to ensure that results are robust with respect to the data sampling.

Fig. 2 shows the results of the grid search and the preferred fault geometries (see Fig. S8 for the initial round of grid search). For comparison, we also include precisely relocated aftershocks (Chen et al. 2025; Yao et al. 2025). Aftershock locations can be useful for constraining the 3-D fault geometry at depth (e.g. Jin and Fialko 2020; Jin et al. 2023), however in case of the Tingri earthquake aftershocks appear to form a diffuse cloud without an obvious localization around the main seismogenic rupture (Fig. 2c–e). Nevertheless, the overall trends of the aftershock hypocenters appear to be broadly consistent with the best-fit fault geometries inferred from inversions of space geodetic data (color dots and black meshes in Fig. 2d–e, respectively).

Early Postseismic Deformation

To investigate the early postseismic deformation, we processed data from Sentinel-1 tracks A12 and D121 spanning ~9 months after the mainshock (Figs. 1 and S3). Our analysis focuses on the amplitude and spatial pattern of surface displacements. Using the first postseismic acquisition as a reference, we generated interferometric pairs with all subsequent acquisitions, for each track. We visually inspected the postseismic interferograms, and selected those that (i) are least affected by decorrelation and atmospheric noise, (ii) maximize the time span, and (iii) have a comparable time span for both tracks. Pairs that fit these criteria are listed in Table S2. To further increase the signal to noise ratio, we stacked the identified long-term interferograms to produce averaged interferograms with time spans of ~8 months for each track. The resulting averaged interferograms are shown in Fig. S3. The postseismic interferograms reveal LOS displacements of several cm (Fig. S3), with a spatial pattern that is broadly consistent with the coseismic one (Fig. S1), suggestive of afterslip as a likely mechanism.

We estimate the distribution of afterslip using the same fault geometry and inversion procedure as for our preferred coseismic slip model. We limit the down-dip extent of the mesh to 15 km to prevent spurious deep slip as the signal-to-noise ratio is poor further than ~ 20 km from the rupture trace (Fig. S3). Because kinematic inversions involve smoothing to reduce non-uniqueness, the inferred area of afterslip may considerably overlap with that of coseismic slip which may be unphysical (Barbot et al. 2009; Lindsey and Fialko 2016). To explore potential trade-offs between model smoothness and resolution, we perform several inversions subject to the following constraints: (i) a soft no-slip boundary condition (Jin and Fialko 2020) at the side and bottom edges of the mesh; no *a priori* constraints on afterslip inside the model domain; (ii) same as (i), but with a soft no-slip boundary condition on mesh elements that produced less than 50% of the peak coseismic slip; (iii) same as (i), but with a soft no-slip boundary condition on mesh elements below the depth of 4 km; (iv) same as (i), but

with a soft no-slip boundary condition on mesh elements in the depth interval 3–11 km. The smoothness parameter of the afterslip model (i) is determined as usual considering a trade-off between the model smoothness and misfit (Fig. S6). For models (ii), (iii), and (iv), the smoothness parameters are chosen to produce the same variance reduction as for model (i). The resulting slip distributions are shown in Figs. 4, S12, and S13.

For completeness, we also perform forward simulations of possible contributions due to viscoelastic and poroelastic deformation. We simulate viscoelastic relaxation using PSGRN-PSCMP software (Wang et al. 2006), assuming the same layered rigidity structure as for the coseismic modeling. The rheology structure includes three layers, an elastic upper crust, a bi-viscous (Burgers) lower crust, and a Maxwell viscoelastic upper mantle, constrained by observations of postseismic deformation due to the 2015 M_w 7.8 Gorkha (Nepal) earthquake (Tian et al. 2020). Because the effective thickness of the upper elastic layer is not well known, we perform calculations assuming elastic thicknesses of 15, 20, 25, and 30 km. In each simulation, we evaluate surface deformation over 3 time intervals: the initial 8 months after the mainshock corresponding to the observation period (Fig. S3 and Table S2), one-half of the Maxwell relaxation time $\tau/2$, and full Maxwell relaxation time $\tau = \eta/\mu$, where η is the dynamic viscosity, and μ is the shear modulus. The computed surface displacements projected on the respective LOS for each satellite track are shown in Figs. 9, 10, and S9-S10.

Results

Our preferred coseismic slip model (Fig. 3) gives rise to a 91% variance reduction of the input data. The 1σ of the residuals for each input data set is shown in Table 1. The model provides a satisfactory fit to all datasets (Fig. 5, Fig. 6). The estimated best-fit average dip angles are $65°\pm5°$ for the main fault and a $70°\pm15°$ for the sub-fault (Fig. 2a,b), which implies optimal orientations for the Mohr-Coulomb failure, assuming vertical orientation of the maximum compressive stress and the coefficient of friction of 0.6-0.7 (e.g. Anderson 1951; Byerlee 1978; Sibson 1974). The fault attitudes inferred from inversions of geodetic data are in general agreement with the distribution of aftershocks (Fig. 2c–e), although the latter are too diffuse to provide robust constraints on the subsurface fault geometry. The moment magnitude calculated using our best-fit slip model (accounting for the depth-dependent shear modulus, Fig. S4) is 7.0, comparable to the seismically determined moment magnitudes using W-phase (7.05, USGS 2025) and centroid-moment tensor (7.1, Ekström et al. 2012), as well as previously published finite fault models (e.g., Qiao et al. 2025).

Coseismic offsets on the main fault are dominated by dip-slip, with some component of left-lateral strike-slip (Fig. 3). Maximum slip (~4.3 m) occurs at a relatively shallow depth of ~6 km. The conjugate sub-fault is also characterized by oblique slip, with a maximum slip of ~1.6 meters at depth of ~5 km (Fig. 3). The total slip amplitude decreases toward the surface, in agreement with field observations of fault scarps with offsets between 1 to 3 meters (Wu et al. 2025). The inferred strike-slip component has a lower resolution and higher uncertainty compared to the dip-slip component, especially for the secondary fault due to a lower signal to noise ratio.

A decrease in coseismic slip towards the surface is further illustrated in Fig. 8, which shows the total coseismic slip averaged along the strike of the main fault, for several depth intervals corresponding to the size of triangular elements (Fig. 3). The shallowest depth interval is constrained to have a constant slip, while the rest of the slip model allows for linear variations in slip between the nodes (see Supplementary Materials). As one can see from Fig. 8, there is a large shallow coseismic slip deficit, with slip at the surface on average almost a factor of 3 smaller than the maximum slip in the middle of the seismogenic zone.

Kinematic inversions of postseismic InSAR data are indicative of the occurrence of early afterslip (Fig. 4). In unconstrained inversions, afterslip is maximum at the surface, but extends to depth of ~10 km, with a substantial spatial overlap with the area of maximum coseismic slip, particularly on the main fault (Fig. 4a). Inversions in which afterslip is discouraged in the area of maximum coseismic slip show a concentration of afterslip on the periphery of the seismic rupture (Fig. 4b). Given that both models are able to explain the observed postseismic deformation with comparable misfits (Fig. 7), we interpret the overlap between the coseismic slip and afterslip as an artifact of the regularization constraint and limited model resolution at depth (Fialko and Kaneko 2025).

While our kinematic afterslip model is able to explain an overall pattern of the observed postseismic deformation, some systematic residuals are apparent (Fig. 7). These

TABLE 1.
1σ for the residual of each track of input data (unit: cm)

Satellite Track	**1σ**
Sentinel-1A ASC12 LOS	8.32
Sentinel-1A DES48 LOS	4.31
Sentinel-1A DES121 LOS	5.54
ALOS-2 DES165 LOS	8.19
LT-1 ASC70 LOS	21.01
Sentinel-1A ASC12 RNG	15.58
Sentinel-1A DES121 RNG	9.89
ALOS-2 DES165 RNG	13.91

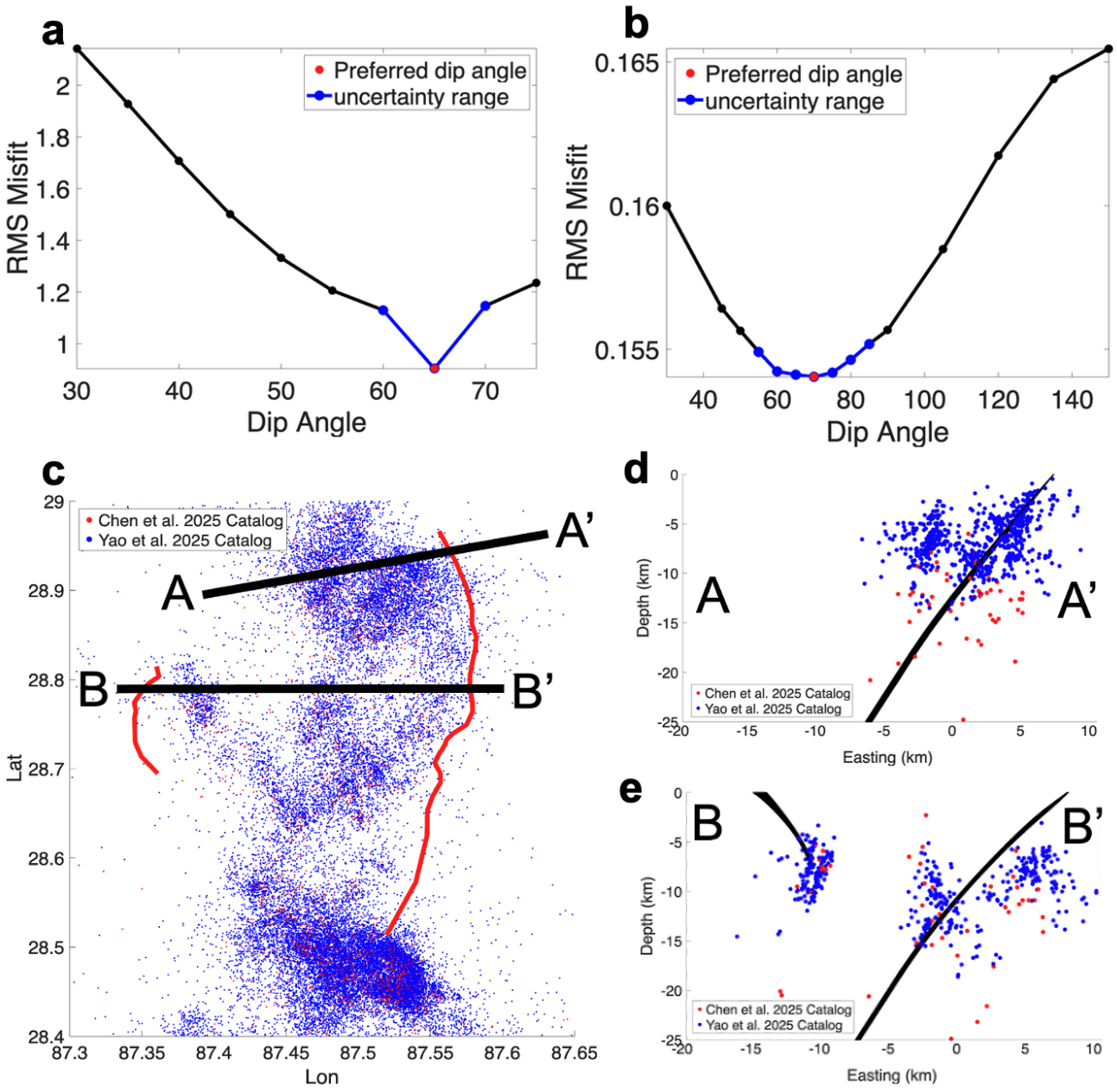

Figure 2. Panels a and b: Model misfit as a function of the assumed fault dip angle. Panel a: main fault; Panel b: sub-fault. Red points represent the best fit (minimum RMS misfit). Blue points represent the estimated uncertainty range (20% and 10% of the difference between the maximum and minimum misfit for the main fault and sub-fault, respectively). Variations in the RMS misfit for the sub-fault are much smaller than those for the main fault because only a small fraction of the data are sensitive to slip on the sub-fault. Panel c: Fault traces and epicenters of precisely relocated aftershocks from Chen et al. (2025) and Yao et al. (2025) catalogs. Panels d–e: cross-sections from profiles A–A' and B–B', with best-fit fault geometries inferred from inversions of space geodetic data (panels a and b) and earthquake hypocenters from Chen et al. (2025) and Yao et al. (2025) catalogs.

Alt-text: Five-panel figure showing dip-angle tests and comparison with relocated aftershock distribution. (a) RMS misfit versus dip angle for the main fault shows a broad U-shaped curve with a red dot marking the minimum at 65 degrees, and blue points marking the preferred uncertainty range. (b) Same plot for the sub-fault, with a narrower U-shape and a minimum near 70 degrees (misfit scale is much smaller than in a). (c) Map of aftershock epicenters from two catalogs (blue and red) overlaid on a fault trace; two profile lines A–A' and B–B' (east-west) cross the cluster. (d–e) Depth–easting cross-sections along A–A' and B–B' showing hypocenter clouds (blue/red) relative to black curves representing inferred fault geometry.

residuals may be due to atmospheric noise and unmodeled ground motion e.g. due to triggered slip on nearby unknown faults (e.g. Ma et al. 2026), landlides, hydrologic effects, etc.

Forward models of viscoelastic relaxation assuming a simple 1-D rheological structure predict LOS displacements that do not agree with observations either in amplitude or the spatial distribution (Figs. 9–10, S9–S10). In particular, the amplitudes of surface displacements predicted by viscoelastic models are about an order of magnitude smaller than the observed ones, assuming an effective elastic thickness of the upper crust of 15 m, and smaller still for thicker elastic layers. The amplitude of surface displacements due to viscoelastic relaxation over a given time period trades off with the assumed effective viscosity, but the spatial pattern of surface displacements varies little in time. It follows that the contribution of viscoelastic relaxation to the observed deformation signal is negligible.

Poroelastic deformation in the limit of full relaxation (Fig. S11) predicts LOS displacements which amplitude and polarity also do not exhibit much similarity with the observations, except perhaps locally near the rupture trace. Taken together, our results point to shallow afterslip as the dominant deformation mechanism in the first 8 months following the Tingri earthquake.

Discussion

Compared to previous studies that approximated the 2025 Tingri rupture using rectangular dislocations in a homogeneous elastic half-space (e.g. Yu et al. 2025; Liu et al. 2025), our finite fault model features a more complex and realistic geometry that honors the curved fault trace at the Earth's surface, and variations in the effective elastic properties with depth. An accurate representation of the fault trace is important as small deviations of the modeled fault trace from the actual surface rupture can result in slivers of data points on the wrong side of the modeled fault, leading to biases in the shallow part of the slip model that in theory should be best resolved by the data. One solution is to simply mask out such data based on the expected sign (e.g. Jin and Fialko 2021); however, adaptation of the more realistic fault geometry obviates the need for discarding potentially useful near-field data. The use of triangular elements ensures a continuous rupture surface without gaps and tears between the adjacent fault elements at depth, while linear base functions ensure a continuous slip distribution. Both features may prove important for dynamic rupture models.

The best-fit dip angles of 60-70 degrees inferred from our non-linear inversions for the main fault and the conjugate sub-fault are consistent with optimal fault orientations predicted by the Mohr-Coulomb theory and Byerlee friction (e.g. Anderson 1951; Collettini and Sibson 2001; Scholz 2019). Shallower dip angles reported in some previous studies (e.g. Yu et al. 2025; Zhao et al. 2025; Chong et al. 2025) could reflect biases due to incomplete data coverage, in particular on the western side of the main fault, which exhibits the largest coseismic displacements, but suffers from decorrelation in the C-band (Sentinel-1) interferograms. Our study mitigates this data gap by using range offsets and L-band (ALOS-2 and LT-1) interferograms that remain correlated all the way to the rupture trace and additionally provide diverse lines of sight. Recent studies that used multiple high-quality data sets (Xu et al. 2025; He et al. 2026) have reported fault dip angles similar to those suggested by our best-fit model.

While faults are generally believed to initiate at optimal angles with respect to in situ principal stresses (e.g. Anderson 1951; Scholz 2019; Fialko 2021), global compilations of earthquake focal mechanisms show a peak in dip angles of normal earthquakes around 45° (e.g. Reston 2020; Jackson and White 1989). Sub-optimal fault orientations can be attributed to a progressive rotation away from the principal compression axis (e.g. Thatcher and Hill 1991; Olive

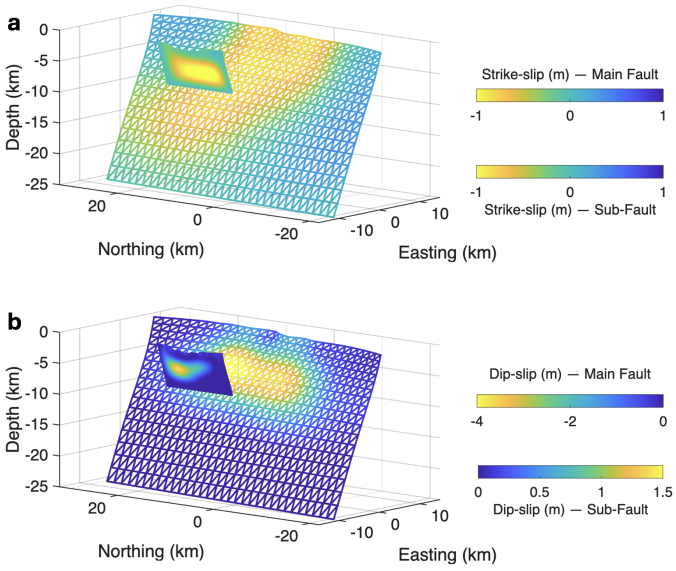

Figure 3. The preferred static slip model from geodetic inversion assuming a curved rupture geometry. Panel a: strike-slip; Panel b: dip-slip. Left-lateral strike slip and west-side-down dip slip are deemed negative.

Alt-text: Two 3-D views of the preferred curved-fault slip solution plotted on triangular meshes in an east–north–depth coordinate system (km). (a) Strike-slip distribution: broader distributed patches on the main fault and a smaller, shallower patch on the sub-fault, each shown with its own color scale (meters). Dominated by left-lateral motion, with slip between 0 and 1 meters. (b) Dip-slip distribution: slip is dominated by normal motion, concentrated in a similar depth range for both faults, but the main fault has higher amplitudes (up to 4 meters) than the sub-fault (lower than 1.5 meters).

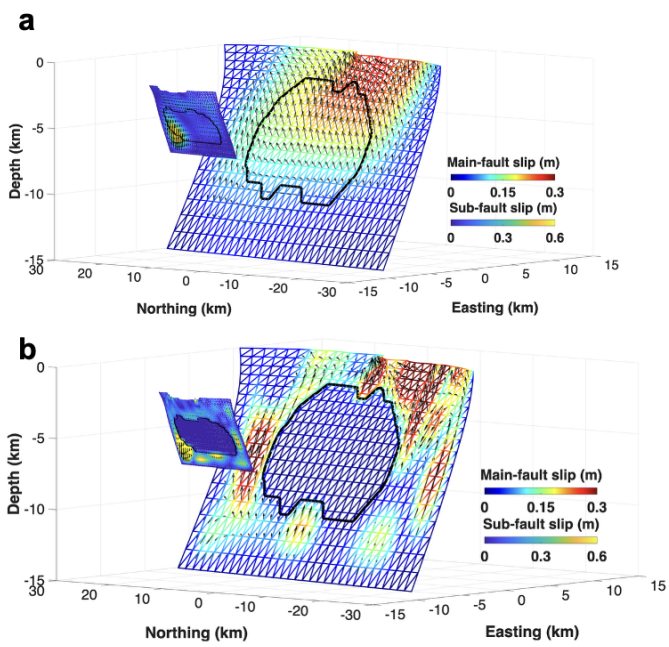

Figure 4. Kinematic inverse models of early afterslip. Black curvy lines represent the contour of the 50% peak coseismic slip for each fault. Panel a: afterslip model with no constraint on the afterslip area; Panel b: afterslip model with slip discouraged inside the 50% peak coseismic slip contour. For the main fault, the arrows represent the movement of the footwall; for the sub-fault, the arrows represent the movement of the hanging wall.

Alt-text: Two 3-D views of early afterslip kinematic inversion results on main and sub-fault meshes (easting, northing, depth). Colored shading shows slip amplitude with separate scales for the main fault (0–0.3 m) and sub-fault (0–0.6 m). Black curving outlines mark the 50 percent peak coseismic-slip contour on each fault. (a) Unconstrained afterslip smoothly distributes across and around the coseismic patch. For main fault the slip concentrates between 0 to 5 km depth. For the sub-fault, the slip concentrates in the north lower corner at a depth of 5-6 meters. (b) Afterslip is suppressed within the contour and concentrates mainly outside/along the patch margins.

and Behn 2014; Fialko and Jin 2021). This would suggest that the Dengmecuo fault that produced the 2025 Tingri earthquake is still relatively young to have avoided a notable rotation, yet sufficiently mature to be able to generate major (magnitude 7+) earthquakes. Similar results were obtained for other major surface-rupturing normal earthquakes for which high-quality space-geodetic data are available (e.g. Kobayashi et al. 2012). Wang et al. (2014) reported dip angles between 40-60 degrees for several M6 normal earthquakes in southern Tibet, and noted that dip angles inferred from inversions of InSAR and teleseismic data may differ by ~10 degrees, especially if the nodal plane ambiguity is

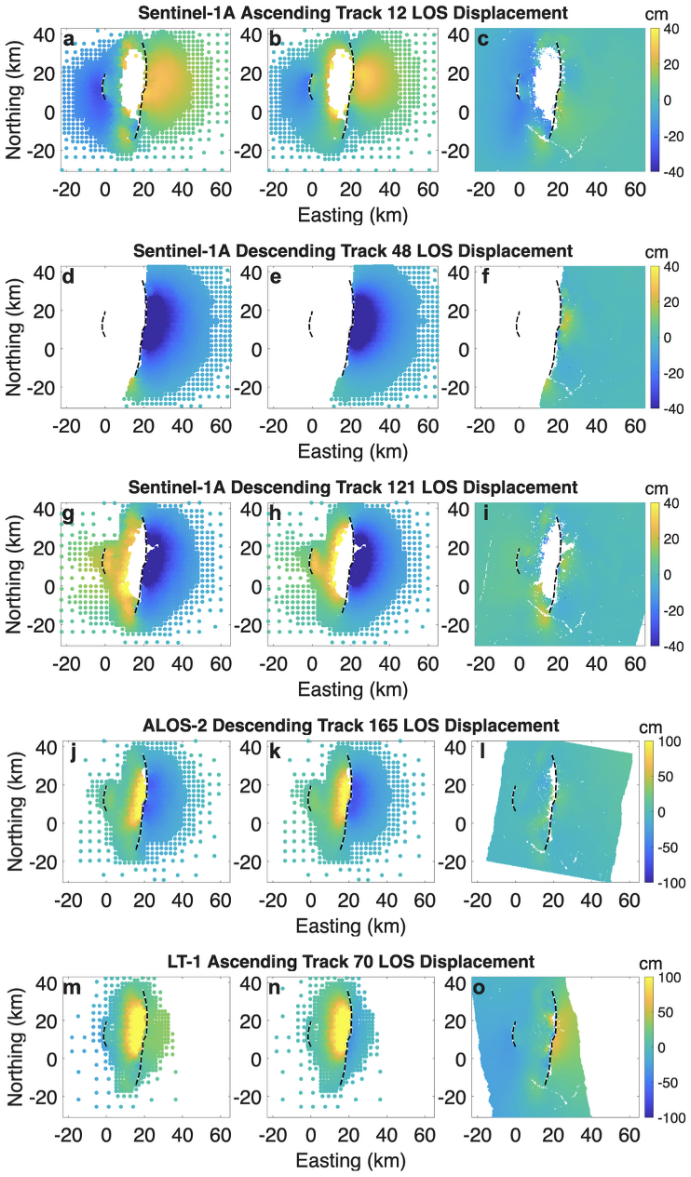

Figure 5. Sub-sampled input data (panels a, d, g, j and m), model prediction (panels b, e, h, k, and n), and full-resolution residual (panels c, f, i, l, and o) for coseismic LOS displacements.

Alt-text: Fifteen-panel comparison of coseismic line-of-sight (LOS) displacement for five sensors/tracks. Rows show Sentinel-1A ascending track 12, Sentinel-1A descending track 48, Sentinel-1A descending track 121, ALOS-2 descending track 165, and Lutan-1 ascending track 70. For each row, the left panel shows sub-sampled LOS observations (colored points), the middle panel shows the corresponding model prediction on the same sample, and the right panel shows the full-resolution residual map. Colors represent LOS displacement (cm) with a strong bipolar lobe across the rupture; residuals are mostly low with localized mismatches near the fault/near masked areas.

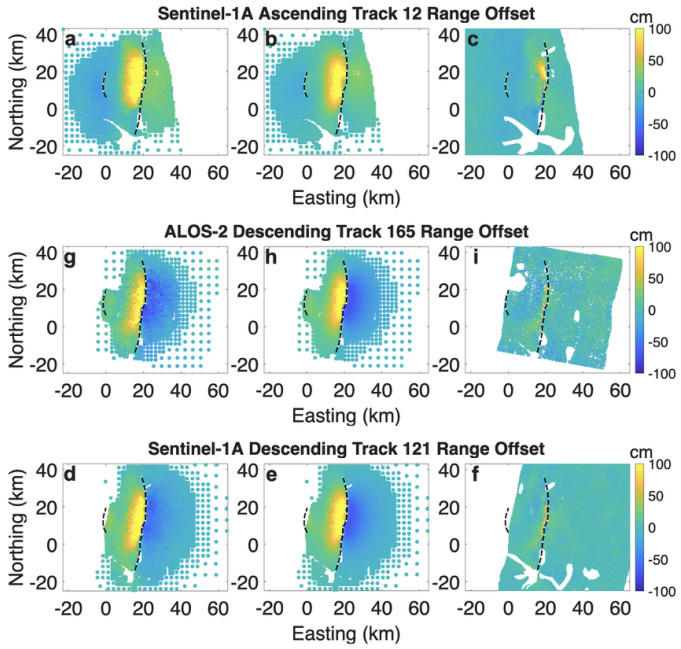

Figure 6. Sub-sampled input data (panels a, d, and g), model prediction (panels b, e, and h), and full-resolution residual (panels c, f, and i) for coseismic range offsets.

Alt-text: Nine-panel comparison of coseismic range offsets for three datasets: Sentinel-1A ascending track 12 (top row), Sentinel-1A descending track 121 (middle row), and ALOS-2 descending track 165 (bottom row). In each row, the left panel shows sub-sampled observations as colored points, the middle panel shows the model prediction at the same points, and the right panel shows the full-resolution residual map. Colors indicate range offset in centimeters (scale -100 to 100 cm). Observations and predictions show a clear positive-negative pattern across the rupture; residuals are mostly small with localized patches near the fault and within/near masked areas.

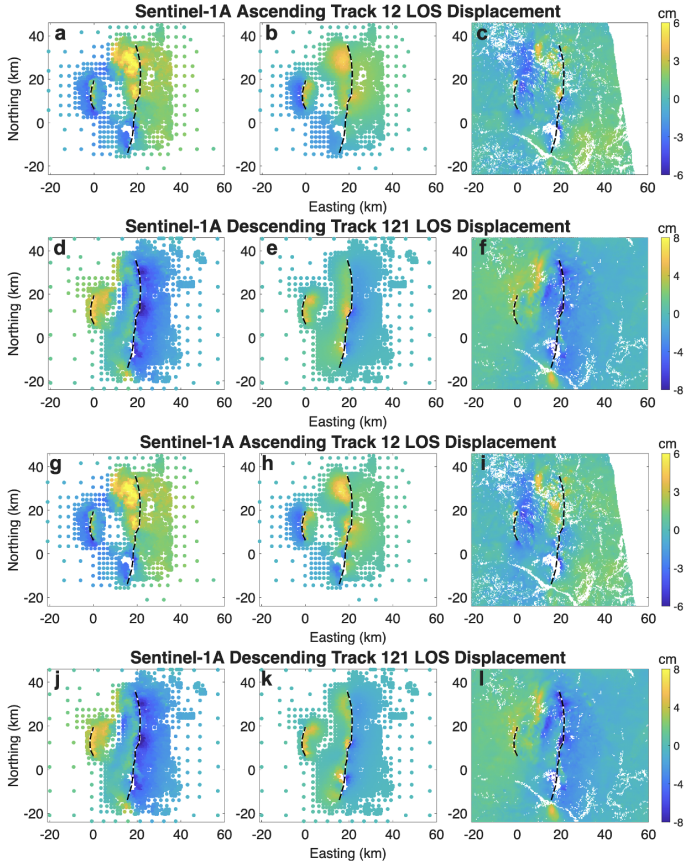

Figure 7. Sub-sampled input data (first column), best-fit afterslip model (second column), and full-resolution residual (third column) for early postseismic deformation. Panels a–f correspond to the afterslip model with no constraint on the afterslip area; Panels g–l correspond to the afterslip model with slip discouraged inside the 50% peak coseismic slip contour.

Alt-text: Twelve map panels of early postseismic Sentinel-1A LOS displacement comparing observations, model, and residuals for two geometries. Rows 1–2 (a–f) use an afterslip model with no constraint on afterslip area; rows 3–4 (g–l) use a model with slip discouraged inside the 50 percent peak coseismic-slip contour. For each track (ascending 12 and descending 121), column 1 shows sub-sampled LOS data (colored points), column 2 shows the best-fit afterslip prediction, and column 3 shows full-resolution residuals. Colors indicate LOS displacement in cm, with masked/blank areas where data are unavailable.

not resolved. A similar discrepancy is found between the dip angles suggested by our geodetic inversions (Fig. 2) and teleseismic data (USGS 2025). This suggests that inferences of non-optimal fault orientation based on earthquake focal mechanisms (Reston 2020; Jackson and White 1989) should be treated with caution.

A classic conjugate orientations of the main fault and the sub-fault (Fig. 2) suggests that the two faults form a graben structure in the Southern Tibet Rift Zone. Their markedly different dimensions suggest they might represent an early-stage graben system that could evolve into a full graben in the future (Qiao et al. 2025). Alternatively, Liu et al. (2025) proposed that the main fault defines a half-graben, and the sub-fault is a "branch rupture" on the opposite side of the Dengmecuo half-graben. Of interest is the slip sequence on the two faults. The earliest post-earthquake SAR data (Table S1) indicate that slip on the sub-fault occurred either simultaneously or within hours following the mainshock. The absence of large aftershocks in the respective time interval and the fact that the sub-fault lies in the static stress shadow of the main fault (Chong et al. 2025) suggest that the sub-fault could have been dynamically triggered and ruptured simultaneously with the mainshock (e.g. Yun et al. 2025).

The high quality observations of coseismic and postseismic deformation due to the 2025 Tingri earthquake provide

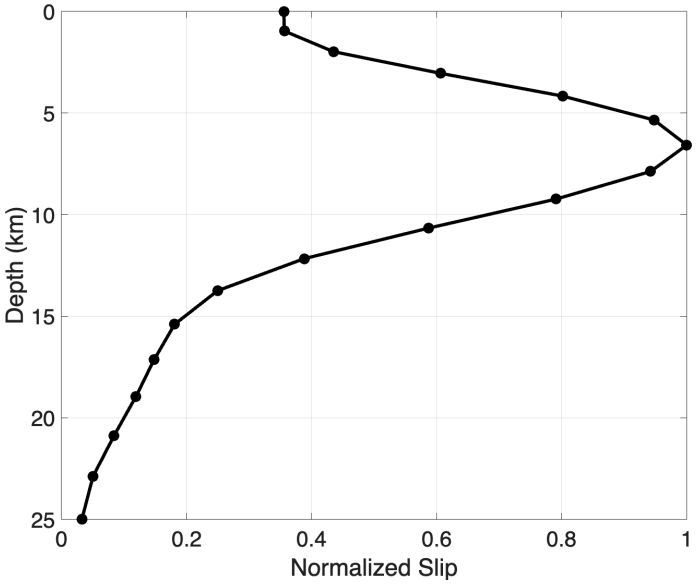

Figure 8. Coseismic slip on the main fault, averaged along-strike, and normalized by the maximum value (~4.3 m), as a function of depth.

Alt-text: Line plot of along-strike–averaged coseismic slip on the main fault versus depth. The x-axis is normalized slip (0 to 1, scaled by a maximum of about 4.3 m) and the y-axis is depth in km (0 at top, increasing to 25 km). Normalized slip is highest (near 1) at shallow depths of roughly 5–8 km, then decreases with depth, dropping below 0.2 by about 15 km depth and approaching near zero at 25 km depth.

an excellent opportunity to investigate contributions of on-and-off fault failure to surface displacements. Our analysis reveals a large (more than a factor of 2) ratio of slip at depth to slip at the surface (Figs. 3 and 8). Similar variations in slip with depth, termed shallow slip deficit (SSD), were inferred for a number of magnitude ~7 earthquakes on strike-slip faults (e.g. Fialko et al. 2005; Jia et al. 2023; Antoine et al. 2024; Milliner et al. 2025; Lindsey et al. 2025). One should be careful to distinguish the shallow coseismic slip deficit (SCSD) from the SSD that was originally defined as the long-term shallow slip deficit (e.g. Fialko et al. 2005; Jin and Fialko 2020), and requires consideration of both coseismic slip and aseismic creep in the interseismic period. So far, no systematic analysis of SSD was performed for normal earthquakes that are large enough to saturate the seismogenic layer.

The reduced coseismic slip and robust afterslip at the Earth's surface (Figs. 3, 8, and 4) are indicative of velocity-strengthening frictional behavior of the shallow crust (e.g. Marone et al. 1991; Scholz 1998). However, a consideration of the magnitudes of the SCSD (>1 meter) and early afterslip (< 10 cm) suggests that the latter may not be able to fully compensate for the former, as the rates of afterslip are highest immediately after the earthquake, and rapidly decay with time (e.g. Marone et al. 1991; Barbot et al. 2009; Lindsey and Fialko 2016). For the estimated slip rate of a few mm/yr and recurrence interval of less than 10^3 years for the Dengmecuo fault (Wu et al. 2025), shallow creep in the interseismic period is unlikely to account for the remaining deficit, given that the rate of shallow creep is typically a small fraction of the long-term fault slip rate (e.g. Savage and Lisowski 1993; Vavra et al. 2023). We thus attribute an apparent SSD to the extensive off-fault damage due to dynamic stress perturbations (e.g. Fialko et al. 2005; Dor et al. 2006; Kaneko and Fialko 2011). A similar combination of the shallow velocity-strengthening layer and off-fault damage was inferred for the 2021 M_w 7.4 Maduo earthquake in the north-eastern Tibetan Plateau (e.g. Jin et al. 2023).

The lack of a clear signal that might be attributable to viscoelastic relaxation in 8 months following the earthquake (Figs 9–10, S9–S10) is consistent with previous estimates of the lower bound on the short-term (transient) viscosity of the lower crust beneath Tibet of the order of 10^{18} Pa s (e.g. Ryder et al. 2011; Wang and Fialko 2018; Tian et al. 2020). Continued space geodetic observations of the Tingri area will provide valuable constraints on the effective rheologic properties of the lower crust and upper mantle beneath the Southern Tibet.

Conclusions

The 2025 M_w 7.1 Tingri earthquake is the largest instrumentally recorded normal earthquake in Southern Tibet. We combined data from several SAR satellites, including Sentinel-1A, ALOS-2 and LT-1, to investigate coseismic and early postseismic deformation due to the Tingri earthquake, and derive a finite fault model. We use a kinematic slip model that allows for complex curved rupture geometries, triangular tesselation, depth-dependent elastic moduli, and piece-wise linear variation in slip components between the mesh nodes. Our best-fit static slip model indicates a 65±5° dip angle for the westward-dipping main fault and a 70±15° for the east-dipping conjugate sub-fault. These dip angles are in excellent agreement with predictions of the Mohr-Coulomb theory assuming Byerlee law and coefficient of friction of 0.6-0.7. The main fault and the sub-fault form a conjugate pair that may define an incipient graben. The coseismic slip distribution is dominated by dip-slip, with some component of left-lateral slip, and a maximum slip of approximately 4 meters on the main fault, and 1.5 meters on the sub-fault. The along-strike averaged slip suggests maximum slip at depth of 5-6 km, and a ~60% shallow coseismic slip deficit. Only a fraction of this deficit is compensated by afterslip in the first 8 months following the earthquake, implying significant off-fault damage, presumably due to strong dynamic stress perturbations. The early postseismic deformation is dominated by afterslip on the ruptured con-

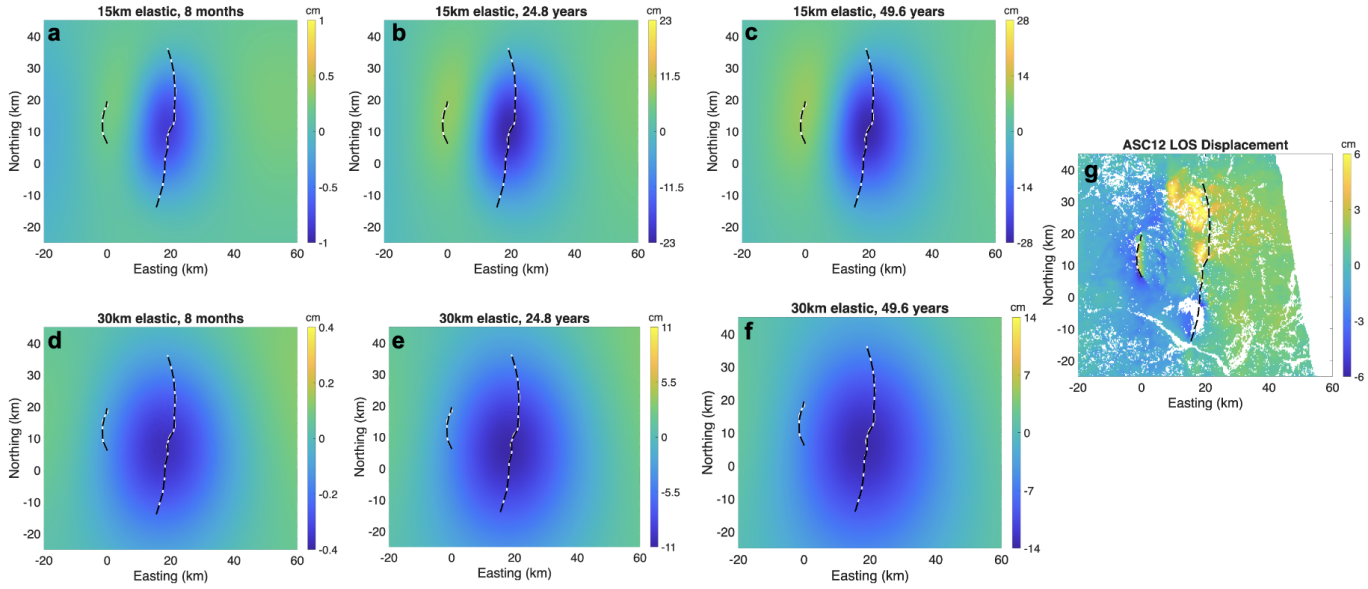

Figure 9. Forward models of viscoelastic relaxation: LOS displacements for Sentinel-1A ascending track 12. Panels a–c: 15 km elastic upper crust thickness, snapshots at 8 months, half Maxwell relaxation time, full Maxwell relaxation time. Panels d–f: 30 km elastic upper crust thickness, snapshots at 8 months, half Maxwell relaxation time, full Maxwell relaxation time. Panel g: observed LOS displacements. The Maxwell relaxation time is calculated based on the regional rigidity and viscosity model of the upper mantle (Huang et al. 2020; Tian et al. 2020).

Alt-text: Seven panels comparing modeled and observed Sentinel-1A ascending track 12 LOS deformation from viscoelastic relaxation forward model. Panels a–c show forward-modeled LOS displacement for a 15 km elastic upper-crust thickness at three times: 8 months, half Maxwell relaxation time (24.8 years), and full Maxwell relaxation time (49.6 years). Panels d–f repeat the three times for a 30 km elastic thickness. Each map uses a cm color scale and shows a broad, smooth, fault-centered LOS lobe that grows in amplitude with time; thicker elastic crust yields smaller amplitudes for the same time snapshot. Panel g shows the observed LOS displacement map for comparison.

jugate faults, with negligible contributions from viscoelastic or poroelastic relaxation. Our results improve understanding of coseismic and postseismic deformation processes in actively extended Earth's crust in the Southern Tibet Rift Zone.

Data and Resources

The supplementary figures and texts are in a separate supplemental material file. The linear geodetic inversion code can be accessed at https://github.com/ZeyuJin/geodetic_inversion. The PSGRM-PSCMP software can be accessed at https://github.com/RongjiangWang/PSGRN-PSCMP_2020. The geodetic data and slip models are accessible via the Zenodo repository: https://zenodo.org/records/18022047.

Declaration of Competing Interests

The authors acknowledge that there are no conflicts of interest.

Acknowledgments

We thank Guest Editor M.-L. Chevalier, H. Wang, and an anonymous reviewer for comments and suggestions that improved this manuscript. Figures were produced using Generic Mapping Tools (GMT) (Wessel et al. 2013) and Matlab.

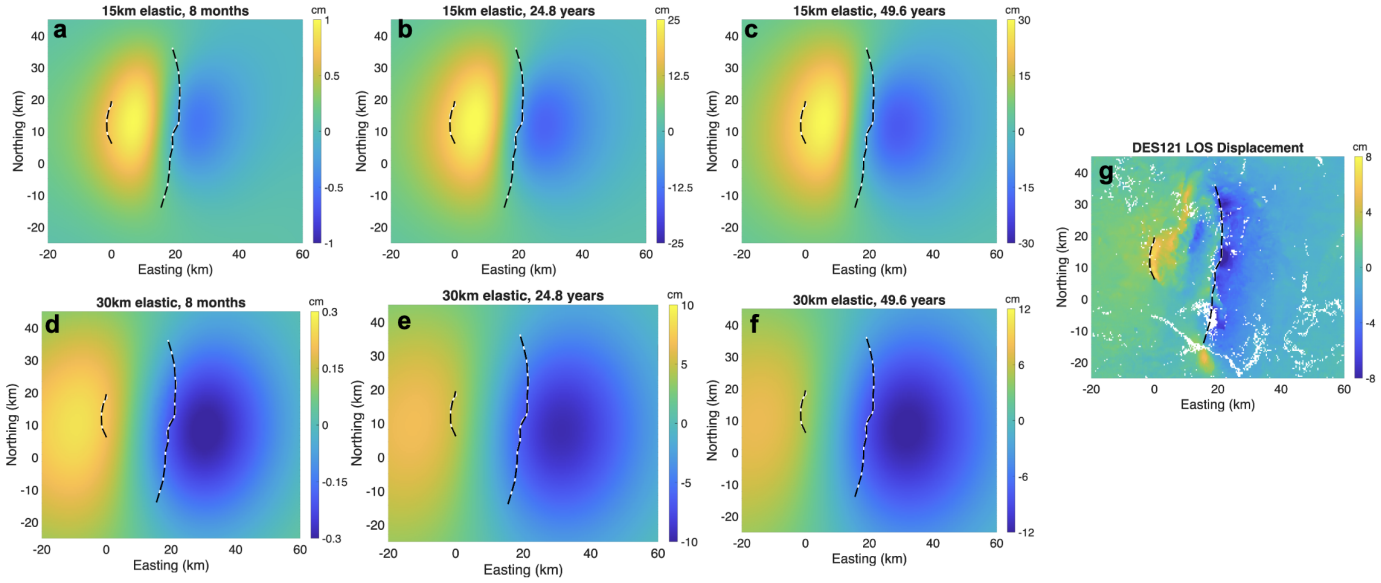

Figure 10. Forward models of viscoelastic relaxation: LOS displacements for Sentinel-1A descending track 121. Panels a–c: 15 km elastic upper crust thickness, snapshots at 8 months, half Maxwell relaxation time, full Maxwell relaxation time. Panels d–f: 30 km elastic upper crust thickness, snapshots at 8 months, half Maxwell relaxation time, full Maxwell relaxation time. Panel g: observed LOS displacements. The Maxwell relaxation time is calculated based on the regional rigidity and viscosity model of the upper mantle (Huang et al. 2020; Tian et al. 2020).

Alt-text: Seven panels comparing modeled and observed Sentinel-1A descending track 121 LOS deformation from viscoelastic relaxation forward model. Panels a–c show forward-modeled LOS displacement for a 15 km elastic upper-crust thickness at three times: 8 months, half Maxwell relaxation time (24.8 years), and full Maxwell relaxation time (49.6 years). Panels d–f repeat the three times for a 30 km elastic thickness. Each map uses a cm color scale and shows a broad, smooth, fault-centered LOS lobe that grows in amplitude with time; thicker elastic crust yields smaller amplitudes for the same time snapshot. Panel g shows the observed LOS displacement map for comparison.

References

Anderson, E. M. (1951). *The dynamics of faulting and dike formation with application to Britain*. Edinburgh: 206 pp., Oliver and Boyd. 5, 7

Antoine, S. L., Y. Klinger, K. Wang, and R. Bürgmann (2024). Coseismic shallow slip deficit accounted for by diffuse off-fault deformation. *Geophys. Res. Lett.* **51**(24), e2024GL110798. 10

Barbot, S., Y. Fialko, and Y. Bock (2009). Postseismic deformation due to the Mw 6.0 2004 Parkfield earthquake: Stress-driven creep on a fault with spatially variable rate-and-state friction parameters. *J. Geophys. Res.* **114**, B07405. 4, 10

Brocher, T. M. (2005). Empirical relations between elastic wavespeeds and density in the earth's crust. *Bulletin of the seismological Society of America* **95**(6), 2081–2092. 4

Byerlee, J. (1978). Friction of rock. *Pure Appl. Geophys.* **116**, 615–626. 5

Chen, K., T. Yang, Y. Z. Wang, X. Y. Guo, J. Zhang, X. Zhang, and R. F. Liu (2025). Quick output parameters related to the 7 January 2025 M6.8 earthquake in Dingri County, Shigatse City, Xizang. *Progress in Earthquake Sciences* **55**(3), 164–171. 4, 6

Chong, Y., D. Dai, X. Li, Y. Wang, Y. Zhang, W. Yang, Y. Han, C. Qu, and L. Meng (2025). Aftershock Triggering Mechanism by the 7 January 2025 Mw 7.1 Tingri Earthquake. *Seismological Research Letters*, 1–13. 2, 7, 9

Collettini, C. and R. H. Sibson (2001). Normal faults, normal friction? *Geology* **29**, 927–930. 2, 7

Dor, O., Y. Ben-Zion, T. Rockwell, and J. Brune (2006). Pulverized rocks in the Mojave section of the San Andreas Fault Zone. *Earth Planet. Sci. Lett.* **245**, 642–654. 10

Dutta, R., S. Jónsson, and H. Vasyura-Bathke (2021). Simultaneous Bayesian estimation of non-planar fault geometry and spatially-variable slip. *J. Geophys. Res.*, e2020JB020441. 2

Ekström, G., M. Nettles, and A. Dziewoński (2012). The global CMT project 2004–2010: Centroid-moment tensors for 13,017 earthquakes. *Physics of the Earth and Planetary Interiors* **200**, 1–9. 5

Farr, T. G., P. A. Rosen, E. Caro, R. Crippen, R. Duren, S. Hensley, M. Kobrick, M. Paller, E. Rodriguez, L. Roth, D. Seal, S. Shaffer, J. Shimada, J. Umland, M. Werner, M. Oskin, D. Burbank, and D. Alsdorf (2007). The shuttle radar topography mission. *Reviews of Geophysics* **45**(2). 2

Fialko, Y. (2004). Probing the mechanical properties of seismically active crust with space geodesy: Study of the coseismic deformation due to the 1992 M_w7.3 Landers (southern California) earthquake. *J. Geophys. Res.* **109**, B03307, 10.1029/2003JB002756. 4

Fialko, Y. (2021). Estimation of absolute stress in the hypocentral region of the 2019 Ridgecrest, California, earthquakes. *J. Geophys. Res.* **126**, e2021JB022000. 2, 7

Fialko, Y. and Z. Jin (2021). Simple shear origin of the cross-faults ruptured in the 2019 Ridgecrest earthquake sequence. *Nat. Geosci.* **14**, 513–518. 8

Fialko, Y. and Y. Kaneko (2025). On the effects of fault alignment on slip stability. *Nature* **642**(8068), E19–E21. 5

Fialko, Y., D. Sandwell, M. Simons, and P. Rosen (2005). Three-dimensional deformation caused by the Bam, Iran, earthquake and the origin of shallow slip deficit. *Nature* **435**, 295–299. 10

Furuya, M. and T. Yasuda (2011). The 2008 Yutian normal faulting earthquake (Mw 7.1), NW Tibet: Non-planar fault modeling and implications for the Karakax Fault. *Tectonophysics* **511**(3-4), 125–133. 2

Goldstein, R. M. and C. L. Werner (1998). Radar interferogram filtering for geophysical applications. *Geophys. Res. Lett.* **25**(21), 4035–4038. 2

Golub, G. H., P. C. Hansen, and D. P. O'Leary (1999). Tikhonov regularization and total least squares. *SIAM journal on matrix analysis and applications* **21**(1), 185–194. 4

Hall, M., A. Lee, C. Cartwright, S. Marahatta, J. Karki, and P. Simkhada (2017). The 2015 Nepal earthquake disaster: lessons learned one year on. *Public Health* **145**, 39–44. 1

He, K., J. Cai, Y. Wen, and C. Xu (2026). Bipartite rupture in the 2025 dingri earthquake indicates normal conjugate faulting during orogenic collapse. *Communications Earth & Environment*. 7

Huang, S., H. Yao, Z. Lu, X. Tian, Y. Zheng, R. Wang, S. Luo, and J. Feng (2020). High-Resolution 3-D shear wave velocity model of the Tibetan Plateau: implications for custal deformation and porphyry Cu deposit formation. *Journal of Geophysical Research: Solid Earth* **125**(7), e2019JB019215. 2, 4, 11, 12

Jackson, J. and N. White (1989). Normal faulting in the upper continental crust: observations from regions of active extension. *Journal of Structural Geology* **11**(1), 15–36. 7, 9

Jia, Z., Z. Jin, M. Marchandon, T. Ulrich, A.-A. Gabriel, W. Fan, P. Shearer, X. Zou, J. Rekoske, F. Bulut, et al. (2023). The complex dynamics of the 2023 Kahramanmaraş, Turkey, M w 7.8-7.7 earthquake doublet. *Science* **381**(6661), 985–990. 10

Jin, Z. and Y. Fialko (2020). Finite slip models of the 2019 Ridgecrest earthquake sequence constrained by space geodetic data and aftershock locations. *Bull. Seism. Soc. Am.* **110**, 1660–1679. 4, 10

Jin, Z. and Y. Fialko (2021). Coseismic and early postseismic deformation due to the 2021 M7.4 Maduo (China) earthquake. *Geophys. Res. Lett.* **48**, e2021GL095213. 7

Jin, Z., Y. Fialko, H. Yang, and Y. Li (2023). Transient deformation excited by the 2021 M7.4 Maduo (China) earthquake: Evidence of a deep shear zone. *J. Geophys. Res.* **128**, e2023JB026643. 4, 10

Jin, Z., Y. Fialko, A. Zubovich, and T. Schöne (2022). Lithospheric deformation due to the 2015 M7.2 Sarez (Pamir) earthquake constrained by 5 years of space geodetic observations. *J. Geophys. Res.* **127**, e2021JB022461. 2

Kaneko, Y. and Y. Fialko (2011). Shallow slip deficit due to large strike-slip earthquakes in dynamic rupture simulations with elasto-plastic off-fault response. *Geophys. J. Int.* **186**, 1389–1403. 10

Kobayashi, T., M. Tobita, M. Koarai, T. Okatani, A. Suzuki, Y. Noguchi, M. Yamanaka, and B. Miyahara (2012). InSAR-derived crustal deformation and fault models of normal faulting earthquake (M_j 7.0) in the Fukushima-Hamadori area. *Earth, planets and space* **64**(12), 1209–1221. 8

Kusky, T. M. and J. Meng (2025). Perspectives on the M 7.1 2025 Southern Tibetan Plateau (Xizang) earthquake. *Journal of Earth Science* **36**(2), 843–846. 1

Li, Y., X. Shan, C. Qu, G. Zhang, X. Wang, and H. Xiong (2025). Slip deficit rate and seismic potential on crustal faults in tibet. *Geophysical Research Letters* **52**(1), e2024GL112122. 2

Lindsey, E. O. and Y. Fialko (2016). Geodetic constraints on frictional properties and earthquake hazard in the Imperial Valley, Southern California. *J. Geophys. Res.* **121**, 1097–1113. 2, 4, 10

Lindsey, E. O., Y.-T. Kuo, Y. Wang, M. Thant, and T. Z. H. Tin (2025). Mature fault mechanics revealed by the highly efficient 2025 mandalay earthquake. *Nature Communications* **16**(1), 10937. 10

Liu, Q., J. Hua, Y. Zhang, W. Gong, J. Zang, G. Zhang, and H. Li (2025). Geodetic observations and seismogenic structures of the 2025 Mw 7.0 Dingri earthquake: The largest normal faulting event in the Southern Tibet Rift. *Remote Sensing* **17**(6). 2, 3, 7, 9

Ma, Z., C. Li, H. Zeng, H. Chen, M. Lyu, Y. Zhang, L. Dal Zilio, X. Shan, and S. Wei (2026). Deciphering stress perturbations throughout the 2025 M w 7.1 Dingri, Southern Xizang Earthquake. *Nature Communications*. 7

Marone, C., C. Scholz, and R. Bilham (1991). On the mechanics of earthquake afterslip. *J. Geophys. Res.* **96**, 8441–8452. 10

McCaffrey, R. and J. Nabelek (1998). Role of oblique convergence in the active deformation of the Himalayas and southern Tibet plateau. *Geology* **26**(8), 691–694. 2

Milliner, C., J. Avouac, J. Dolan, and J. Hollingsworth (2025). Localization of inelastic strain with fault maturity and effects on earthquake characteristics. *Nature Geoscience* **18**, 793–800. 10

Molnar, P., P. England, and J. Martinod (1993). Mantle dynamics, uplift of the Tibetan Plateau, and the Indian Monsoon. *Reviews of Geophysics* **31**(4), 357–396. 2

Nikkhoo, M. and T. R. Walter (2015). Triangular dislocation: an analytical, artefact-free solution. *Geophysical Journal International* **201**(2), 1119–1141. 2

Olive, J.-A. and M. D. Behn (2014). Rapid rotation of normal faults due to flexural stresses: An explanation for the global distribution of normal fault dips. *J. Geophys. Res.* **119**(4), 3722–3739. 7

Pang, Y., H. Zhang, T. V. Gerya, J. Liao, H. Cheng, and Y. Shi (2018). The mechanism and dynamics of N-S rifting in Southern Tibet: Insight From 3-D thermomechanical modeling. *Journal of Geophysical Research: Solid Earth* **123**(1), 859–877. 2

Qi, L., L. ChengTao, Z. Bin, H. Yong, W. YongGe, T. Kai, and D. Qing (2024). Estimated seismic source parameters for 2020 Dingri Mw 5.6 earthquake in Xizang and study on the stress triggering. *Chinese Journal of Geophysics (in Chinese)* **67**(1), 172–188. 1

Qiao, X., Z. Lu, S. Yan, H. Shi, M. Zhi, and D. Zhao (2025). The 2025 MW7.0 Dingri earthquake: conjugate normal faulting of a graben structure in the Southern Xainza-Dinggye Rift. *Geophysical Research Letters* **52**(12), e2025GL116154. 2, 5, 9

Reston, T. (2020). On the rotation and frictional lock-up of normal faults: Explaining the dip distribution of normal fault earthquakes and resolving the low-angle normal fault paradox. *Tectonophysics* **790**, 228550. 7, 9

Ryder, I., R. Bürgmann, and F. Pollitz (2011). Lower crustal relaxation beneath the Tibetan Plateau and Qaidam Basin following the 2001 Kokoxili earthquake. *Geophys. J. Int.* **187**(2), 613–630. 10

Sandwell, D., R. Mellors, X. Tong, M. Wei, and P. Wessel (2011). Open radar interferometry software for mapping surface deformation. *EOS, Trans. AGU* **92**(28), 234–234. 2

Savage, J. and M. Lisowski (1993). Inferred depth of creep on the Hayward fault, central California. *J. Geophys. Res.* **98**, 787–793. 10

Scholz, C. H. (1998). Earthquakes and friction laws. *Nature* **391**, 37. 10

Scholz, C. H. (2019). *The mechanics of earthquakes and faulting*. New York, NY: 3rd Ed., 493 pp., Cambidge Univ. Press. 2, 7

Sibson, R. H. (1974). Frictional constraints on thrust, wrench and normal faults. *Nature* **249**, 542–544. 5

Simons, M., Y. Fialko, and L. Rivera (2002). Coseismic deformation from the 1999 M_w7.1 Hector Mine, California, earthquake, as inferred from InSAR and GPS observations. *Bull. Seism. Soc. Am.* **92**, 1390–1402. 2

Tan, P., X. Liang, W. Li, and C. Wu (2023). Crustal structure of the tibetan plateau and adjacent areas revealed from ambient noise tomography. *Gondwana Research* **121**, 1–15. 2

Thatcher, W. and D. P. Hill (1991). Fault orientations in extensional and conjugate strike-slip environments and their implications. *Geology* **19**, 1116–1120. 7

Tian, Z., J. T. Freymueller, and Z. Yang (2020). Spatio-temporal variations of afterslip and viscoelastic relaxation following the Mw7.8 Gorkha (Nepal) earthquake. *Earth Planet. Sci. Lett.* **532**, 116031. 5, 10, 11, 12

USGS (2025). M 7.1 - 2025 Southern Tibetan Plateau Earthquake. https://earthquake.usgs.gov/earthquakes/eventpage/us6000pi9w/executive. Accessed: 2025-11-23. 1, 2, 5, 9

Vavra, E. J., H. Qiu, B. Chi, P.-E. Share, A. Allam, M. Morzfeld, F. Vernon, Y. Ben-Zion, and Y. Fialko (2023). Active dipping interface of the Southern San Andreas fault revealed by space geodetic and seismic imaging. *J. Geophys. Res.* **128**, e2023JB026811. 10

Wang, H., J. R. Elliott, T. J. Craig, T. J. Wright, J. Liu-Zeng, and A. Hooper (2014). Normal faulting sequence in the Pumqu-Xainza Rift constrained by InSAR and teleseismic body-wave seismology. *Geochemistry, Geophysics, Geosystems* **15**(7), 2947–2963. 8

Wang, K. and Y. Fialko (2015). Slip model of the 2015 M_w 7.8 Gorkha (Nepal) earthquake from inversions of ALOS-2 and GPS data. *Geophys. Res. Lett.* **42**, 7452–7458. 3

Wang, K. and Y. Fialko (2018). Observations and modeling of co- and postseismic deformation due to the 2015 M_w 7.8 Gorkha (Nepal) earthquake. *J. Geophys. Res.* **123**(1), 761–779. 1, 10

Wang, R., F. Lorenzo-Martin, and F. Roth (2006). PSGRN/PSCMP-a new code for calculating co- and post-seismic deformation, geoid and gravity changes based on the viscoelastic-gravitational dislocation theory. *Comp. Geosci.* **32**, 527–541. 4, 5

Wang, T. and S. Jónsson (2014). Phase-ramp reduction in interseismic interferograms from pixel-offsets. *IEEE Journal of Selected Topics in Applied Earth Observations and Remote Sensing* **7**(5), 1709–1718. 2

Wessel, P., W. H. F. Smith, R. Scharroo, J. Luis, and F. Wobbe (2013). Generic Mapping Tools: Improved Version Released. *Eos, Trans. AGU* **94**, 409–410. 11

Wu, K., M.-L. Chevalier, J. Pan, F. Liu, S. Yang, S. Zhang, Q. Su, and H. Li (2025). Recurrence of large earthquakes along the southern Xainza-Dinggye rift and comparison with the 7 January 2025, Mw7.1 Tingri earthquake, southern Tibet. *Tectonophysics* **910**, 230827. 5, 10

Wu, X., X. Xu, G. Yu, J. Ren, X. Yang, G. Chen, C. Xu, K. Du, X. Huang, H. Yang, K. Li, and H. Hao (2024). The China Active Faults Database (CAFD) and its web system. *Earth System Science Data* **16**(7), 3391–3417. 3

Xu, W., C. Bai, C. Huang, R. Bürgmann, B. Shan, X. Shan, Z. Chen, L. Xie, and F. Shi (2025). Northward rupture and early afterslip of two graben-bounding normal faults during the 2025 dingri earthquake of tibet. *Communications Earth & Environment*. 7

Yang, J., Y. Wen, C. Xu, and Q. Hu (2025, 09). Complex multifault rupture during the 2016–2025 Dingri earthquakes, Southern Tibetan Plateau, inraveled by ,ultisource InSAR observations. *Seismological Research Letters*. 2

Yao, J., D. Yao, F. Chen, M. Zhi, L. Sun, and D. Wang (2025). A preliminary catalog of early aftershocks following the 7 January 2025 Ms 6.8 Dingri, Xizang earthquake. *Journal of Earth Science* **36**(2), 856–860. 4, 6

Yu, C., Z. Li, X. Hu, C. Song, S. Li, H. Liu, J. Li, B. Han, Z. Liu, M. Liu, S. Zhu, X. Hao, Z. Li, and J. Peng (2025). Source parameters and induced Hazards of the 2025 Mw 7.1 Dingri earthquake on the Southern Tibetan Plateau (Xizhang), China, as revealed by imaging geodesy. *Journal of Earth Science* **36**(2), 847–851. 1, 2, 7

Yu, S., S. Zhang, J. Luo, Z. Li, and J. Ding (2025). The tectonic significance of the M w7. 1 earthquake source model in Tibet in 2025 constrained by InSAR data. *Remote Sensing* **17**(5), 936. 2, 7

Yun, J., A.-A. Gabriel, D. A. May, and Y. Fialko (2025). Controls of dynamic and static stress changes and aseismic slip on delayed earthquake triggering: Application to the 2019 Ridgecrest earthquake sequence. *J. Geophys. Res.* **130**(12), e2025JB031271. 9

Zhang, Y., H. Fattahi, and F. Amelung (2019). Small baseline insar time series analysis: Unwrapping error correction and noise reduction. *Computers & Geosciences* **133**, 104331. 2

Zhao, X., Z. Xiao, W. Wang, and J. Li (2025). Along-strike variation of the unilateral rupture of the 2025 mw7.1 Dingri, Xizang earthquake: One of the shallowest m7+ normal-faulting events on the Tibetan Plateau. *Geophys. Res. Lett.* **52**(23), e2025GL119397. 7

Zhou, J. and L. Li (2025). An open access 90 m resolution VS30 data and map for areas affected by the January 2025 M6.8 Dingri Xizang, China earthquake. *Earthquake Science* **38**(4), 1–7. 1

Zhu, J., B. Zhang, S. Yao, and Y. Cai (2025). Coseismic deformation, fault slip distribution, and stress changes of the 2025 MS

6.8 Dingri earthquake from Sentinel-1A InSAR observations. *Geosciences* **15**(11), 421. 2

Zou, X., Y. Fialko, A. Dennehy, A. Cloninger, and S. J. Semnani (2023). High-angle active conjugate faults in the Anza-Borrego Shear Zone, Southern California. *Geophys. Res. Lett.* **50**, e2023GL105783. 2

Corresponding author (Xiaoyu Zou) mailing address: 8800 Biological grade, La Jolla, CA, 92037, USA

Manuscript Received 00 Month 0000

Supplemental Information for "The 2025 M_w 7.1 Tingri (South Tibet) Earthquake: Rupture of Normal Conjugate Optimally Oriented Faults, Shallow Coseismic Slip Deficit, and Early Afterslip"

Xiaoyu Zou[1] and Yuri Fialko[1]

[1]Institute of Geophysics and Planetary Physics, Scripps Institution of Oceanography, University of California San Diego, La Jolla, 92093, CA, USA.

Contributing authors: x3zou@ucsd.edu; yfialko@ucsd.edu;

Contents of this file

Text S1. Inversion of Geodetic Data for Static Slip Model

Inversions of coseismic displacements for subsurface slip typically represent faults as superposed dislocations [1–3]. Rectangular dislocations in homogeneous [4] or layered [5] half-spaces are common; TDEs better capture non-planar geometries [6–8]. Because finite dislocations yield piece-wise constant ("staircase") slip, we invert surface displacements using piece-wise linear triangular boundary elements in a layered elastic half-space to obtain continuous slip.

We first tessellate the 3-D fault surface (Fig. 3) into a watertight triangular mesh whose element size increases from ∼1 km at the surface to ∼5 km at depth (20–25 km), keeping the resolution matrix near diagonal [9]. Each triangle is modeled by a superposition of equally spaced point sources [8]. Green's functions assume the 1-D rigidity profile in Fig. S4; for elements at the free surface we use TDEs [7] to avoid near-field singularities. For each triangle vertex, we compute Green's functions by prescribing unit slip at that vertex with a linear taper to zero at vertices of adjacent triangles—analogous to linear basis functions in FEM [10]. We then solve for nodal slip u on the mesh vertices from $Gu = d$, where G projects 3-component displacements onto the LOS and range offset observations from Sentinel-1, ALOS-2, and LT-1 collected in d; u contains strike- and dip-slip components per node.

$$F(u, \lambda) = ||Gu - d||_2 + \lambda ||\nabla^2 u||_2, \tag{1}$$

with $||\cdot||2$ the Euclidean norm and ∇^2 a Laplacian smoothness penalizing curvature [11]; λ is selected by L-curve trade-off (Fig. S5, S6). The discrete Laplacian on the triangular mesh uses an edge-hybrid scheme: cotangent weights for acute triangles and mean-value weights otherwise [12]. For neighboring nodes i and j sharing edge ij (Fig. S7), with opposite angles $\theta ikj, \theta_{ilj}$ and vertices k, l, and positions $\mathbf{p}_i, \mathbf{p}_j$,

$$w_{ij} = \begin{cases} \frac{1}{2}\big(\cot\theta_{ikj} + \cot\theta_{ilj}\big), & \text{if } \theta_{ikj}, \theta_{ilj} \in (0, \frac{\pi}{2}) \text{ (both acute)}, \\ \dfrac{\tan(\theta_{kij}/2) + \tan(\theta_{lij}/2) + \tan(\theta_{kji}/2) + \tan(\theta_{lji}/2)}{\|\mathbf{p}_i - \mathbf{p}_j\|}, & \text{otherwise}, \end{cases} \tag{2}$$

and the node-wise operator is [12]

$$\nabla^2 u_i = \frac{1}{S_i} \sum_{j=1}^{N} w_{ij}(u_j - u_i), \tag{3}$$

where S_i is the mixed-Voronoi area [13;14] around node i (Fig. S7), assembled from triangle-wise contributions for triangle T (vertices i, j, k, area A_T):

$$S_i^{(T)} = \begin{cases} \dfrac{1}{8}\big(\cot\theta_{ijk}\,\|\mathbf{p}_i - \mathbf{p}_k\|^2 + \cot\theta_{ikj}\,\|\mathbf{p}_i - \mathbf{p}_j\|^2\big), & \text{if } T \text{ is non-obtuse}, \\ \dfrac{1}{2} A_T, & \text{if } \theta_{kij} > \frac{\pi}{2} \text{ (obtuse at } i), \\ \dfrac{1}{4} A_T, & \text{if } T \text{ is obtuse at } j \text{ or } k. \end{cases} \tag{4}$$

In a multi-fault setting where there are two faults with huge differences in mesh sizes, a single regularization strength may act unevenly: one fault can be over-smoothed and another under-smoothed. We apply a normalization process to the smoothness matrix, which is to scale the operator by the median edge length, removing the mesh-dependent bias so that the penalty measures roughness consistently.

The design matrix stacks G with a symmetric, sparse regularizer that independently smooths strike- and dip-slip. TDEs at the top are tied to the top nodes of the linear triangular elements below, and we impose soft zero-slip at lateral and basal boundaries [15]. Inversions use the SlipSolve package [16].

Satellite	Track	Orbit	Acquisition dates	$B_\perp$ (m)
ALOS-2	165	descending	2024/10/15 – 2025/01/08	60
Sentinel-1A	48	descending	2024/12/27 – 2025/01/08	49
Sentinel-1A	121	descending	2025/01/01 – 2025/01/13	15
Sentinel-1A	12	ascending	2025/01/05 – 2025/01/17	50
LT-1	70	ascending	2024/12/06 – 2025/01/07	551

Table S1: SAR data used in coseismic slip modeling. $B_\perp$ is a perpendicular baseline between the respective repeat orbits.

Satellite	Track	Orbit	Acquisition dates	$B_\perp$ (m)
Sentinel-1A	12	ascending	2025/01/17 – 2025/09/02	122
Sentinel-1A	12	ascending	2025/01/17 – 2025/09/14	218
Sentinel-1A	12	ascending	2025/01/17 – 2025/09/26	81
Sentinel-1A	121	descending	2025/01/13 – 2025/09/10	31
Sentinel-1A	121	descending	2025/01/13 – 2025/09/22	93

Table S2: SAR data used in early postseismic slip modeling. $B_\perp$ is a perpendicular baseline between the respective repeat orbits. The input data is the stack of ascending and descending tracks from the table above.

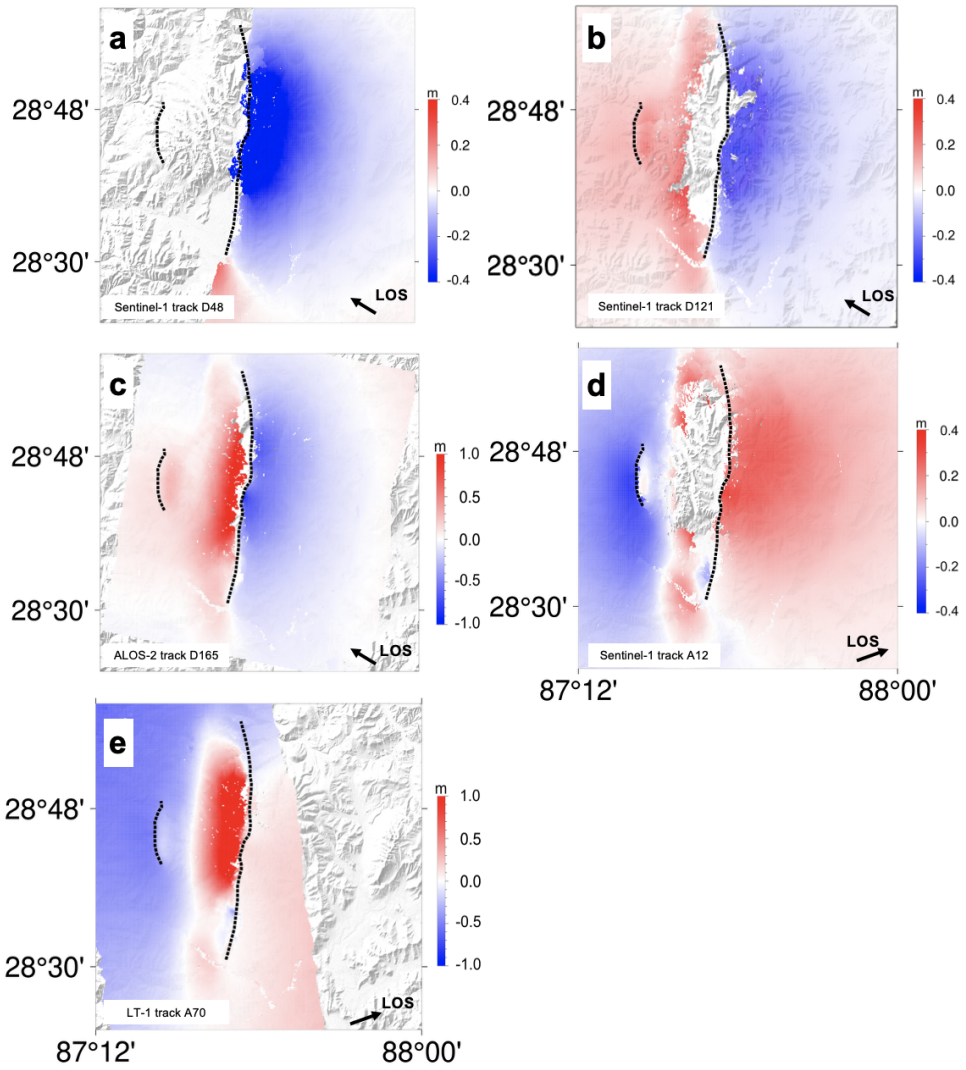

Fig. S1: The line-of-sight displacement data used for coseismic slip model inversion. All panels share the same spatial coverage.

Alt-text: Five LOS displacement maps with identical geographic coverage showing coseismic deformation used for slip inversion from multiple sensors/tracks. Panels a–e display Sentinel-1 descending track D48, Sentinel-1 descending track D121, ALOS-2 descending track D165, Sentinel-1 ascending track A12, and Lutan-1 ascending track A70. Colors show LOS displacement in meters (red positive, blue negative) with a strong two-lobed signal separated by the mapped fault trace (black dashed line); a smaller nearby fault trace is also shown. Each panel includes an LOS look-direction arrow and a color bar (plus and minus 0.4 m for Sentinel-1 panels; plus and minus 1.0 m for ALOS-2 and Lutan-1).

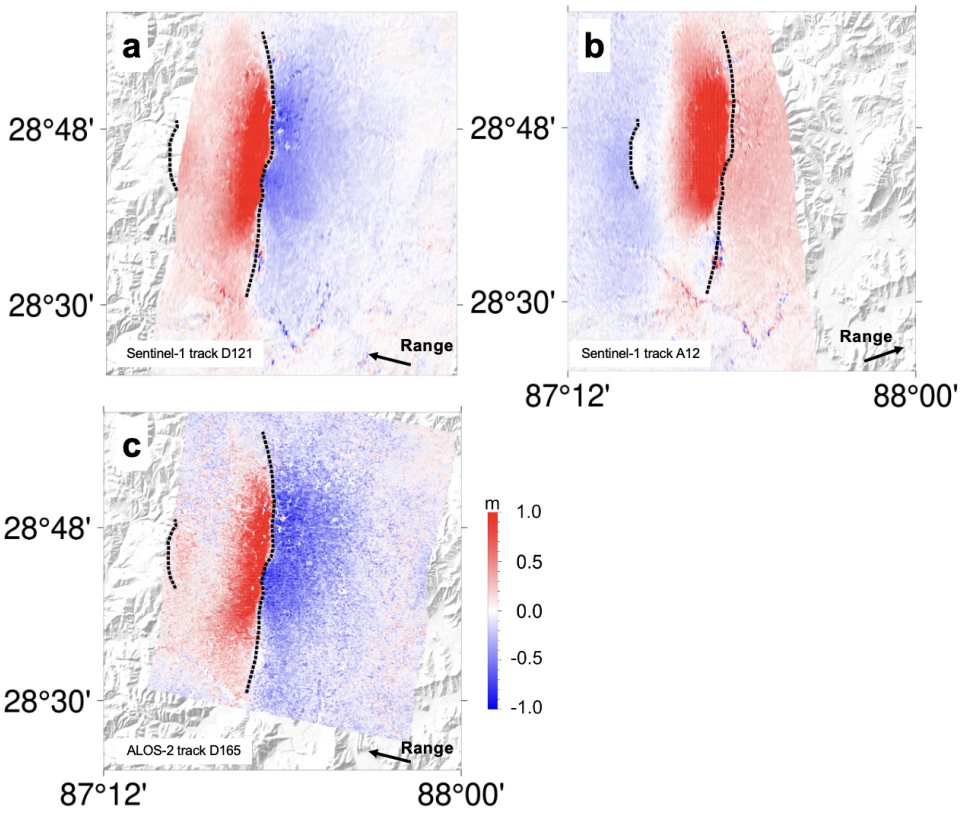

Fig. S2: The range offset data used for coseismic slip model inversion. All panels share the same spatial coverage and colorbar range.

Alt-text: Three maps of coseismic range offsets used for slip inversion, all with the same map extent and the same color scale (meters, -1.0 to 1.0). Panels a–c show Sentinel-1 descending track D121, Sentinel-1 ascending track A12, and ALOS-2 descending track D165. Colors (red positive, blue negative) form a strong two-lobed pattern on either side of the mapped fault trace (black dashed line), with a smaller nearby fault segment also shown. Each panel includes a range-direction arrow indicating the measurement direction.

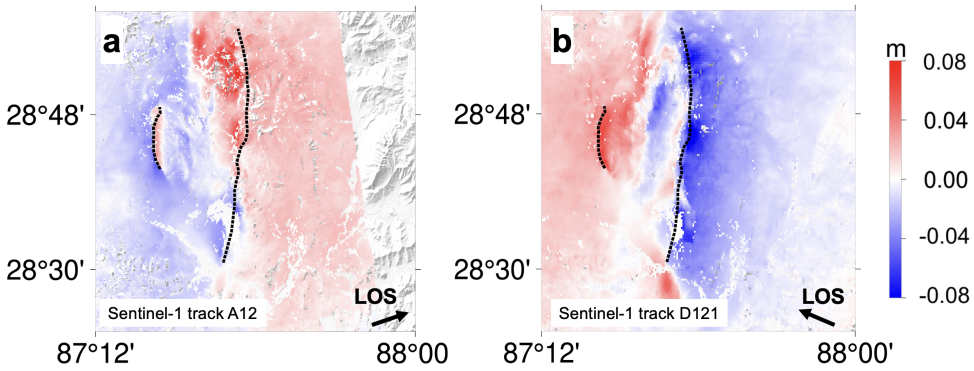

Fig. S3: The line-of-sight displacement data used for postseismic slip model inversion. All panels share the same spatial coverage and colorbar range.

Alt-text: Two LOS displacement maps used for postseismic slip inversion with identical spatial coverage and a shared color scale (meters, -0.08 to 0.08). Panel a shows Sentinel-1 ascending track A12 and panel b shows Sentinel-1 descending track D121. Colors (red positive, blue negative) outline a narrow, fault-parallel deformation signal centered on the mapped fault trace (black dashed line), and each panel includes an LOS look-direction arrow.

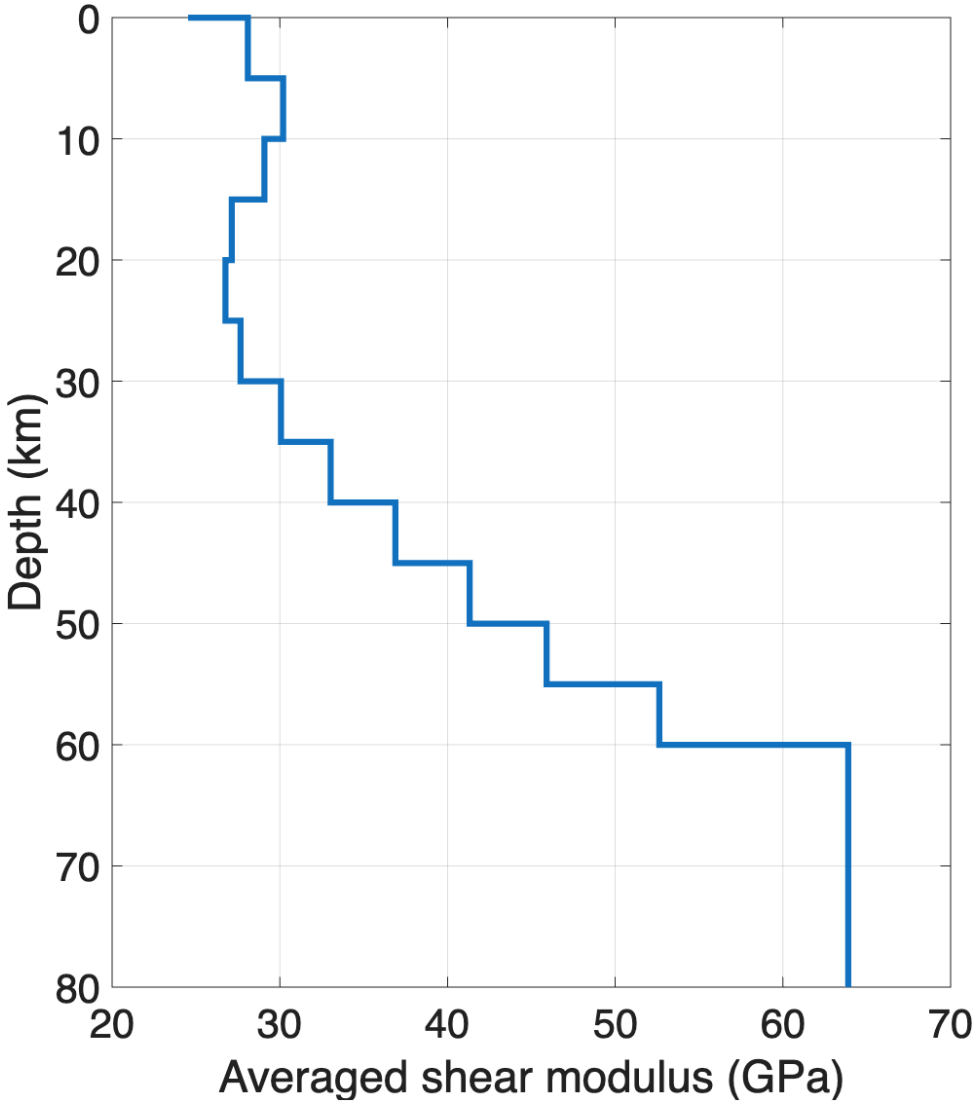

Fig. S4: The 1-D layered rigidity model for constructing the hybrid Green's function.

Alt-text: Stepwise depth profile of the 1-D layered rigidity structure used to build the hybrid Green's function. The x-axis shows averaged shear modulus (GPa) and the y-axis shows depth (km, increasing downward to 80 km). Shear modulus is about 25–30 GPa in the shallow crust, increases gradually through the mid- to lower crust (about 30–45 GPa by around 40–50 km), and reaches higher values in the upper mantle (about 50–65 GPa below around 55–60 km).

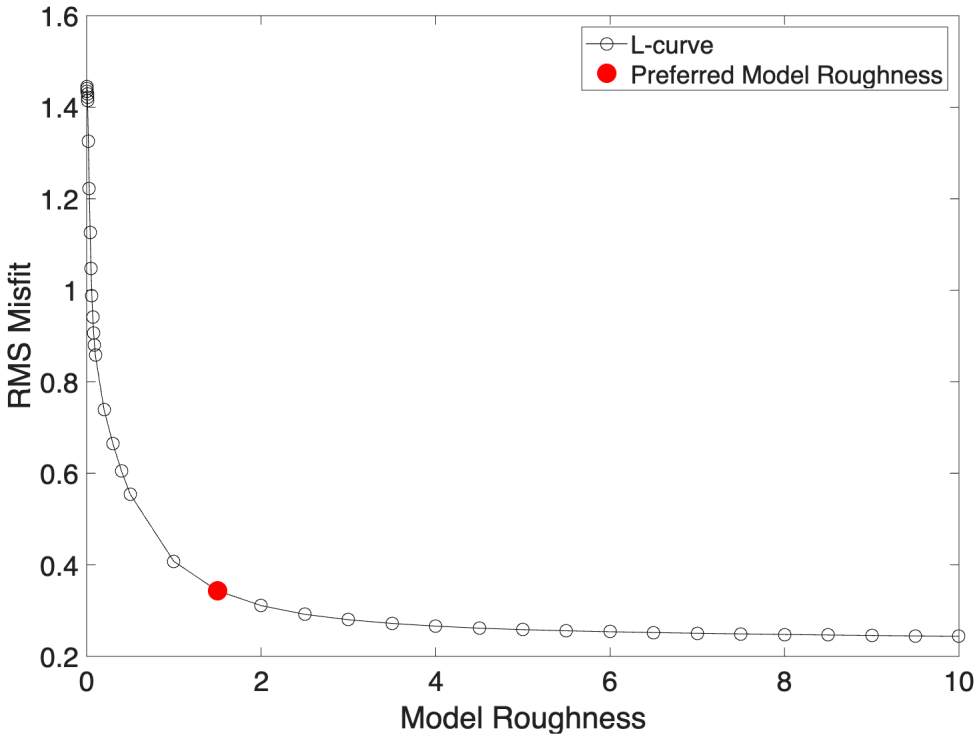

Fig. S5: The roughness-misfit trade-off curve for selecting the preferred model smoothness of the coseismic slip model.

Alt-text: Roughness–misfit trade-off (L-curve) used to choose smoothing for the coseismic slip inversion. The x-axis is model roughness and the y-axis is RMS misfit. The curve drops steeply from high misfit at very low roughness to a broad, nearly flat region where additional roughness yields only small misfit improvement. A red marker highlights the selected preferred model roughness near the curve's elbow.

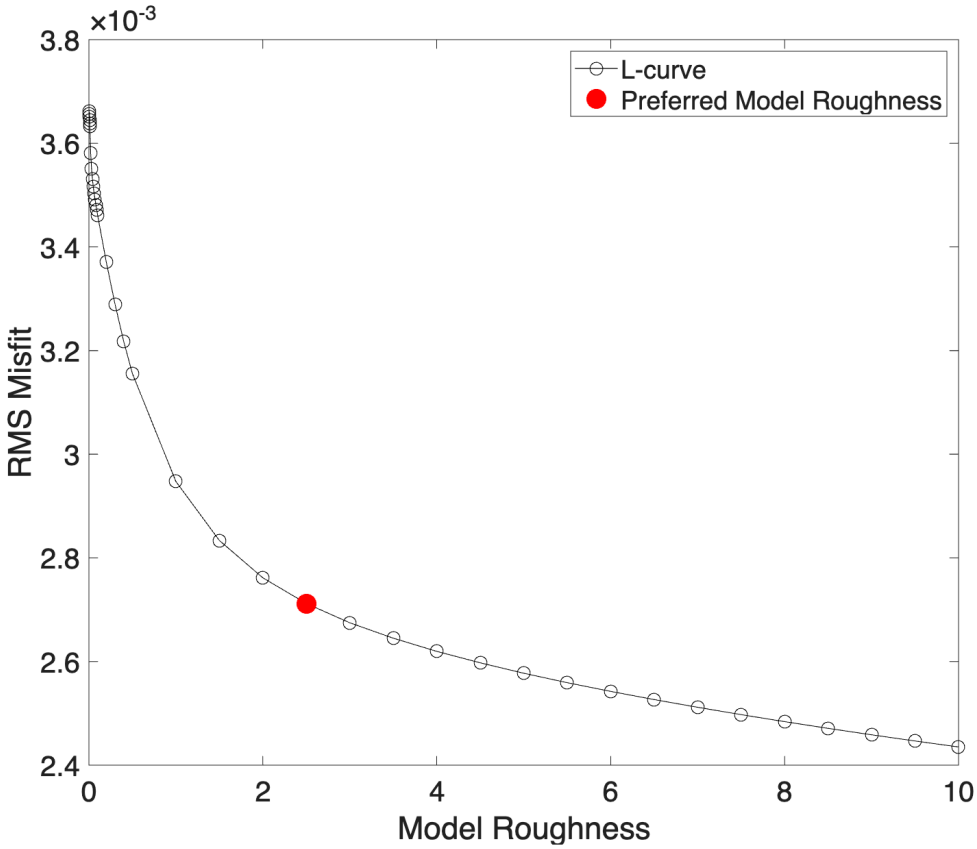

Fig. S6: The roughness-misfit trade-off curve for selecting the preferred model smoothness of the unconstrained postseismic slip model.

Alt-text: Roughness–misfit trade-off (L-curve) used to choose smoothing for the unconstrained postseismic slip inversion. The x-axis is model roughness and the y-axis is RMS misfit. The curve drops steeply from high misfit at very low roughness to a broad, nearly flat region where additional roughness yields only small misfit improvement. A red marker highlights the selected preferred model roughness near the curve's elbow.

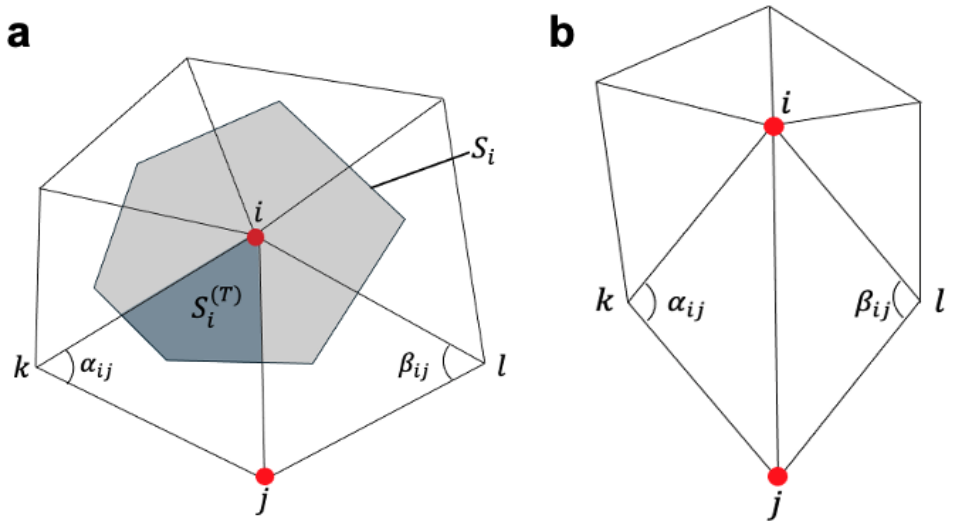

Fig. S7: Illustration of Laplacian weighting schemes for acute (panel a) and obtuse (panel b) triangles. S_i denotes the Voronoi cell area in the case when none of the triangles are obtuse. The dark-shaded area $S_i^{(T)}$ represents the Voronoi cell of an individual triangle ijk, part of the total Voronoi cell S_i of node i.

Alt-text: Schematic of Laplacian weighting for a mesh node i using Voronoi-cell areas, comparing an acute triangle and an obtuse triangle. (a) Acute case: node i (red point) connects to neighboring nodes including j, with angles alpha ij and beta ij indicated at adjacent corners. A light-gray polygon labeled Si represents the full Voronoi cell area around node i for a non-obtuse triangulation, and a dark shaded sector Si-T shows the contribution from one triangle ijk to Si. (b) Obtuse case: an obtuse triangle with nodes i and j highlighted (red), and angles alpha ij and beta ij marked, illustrating how the weighting geometry changes when the triangle is obtuse.

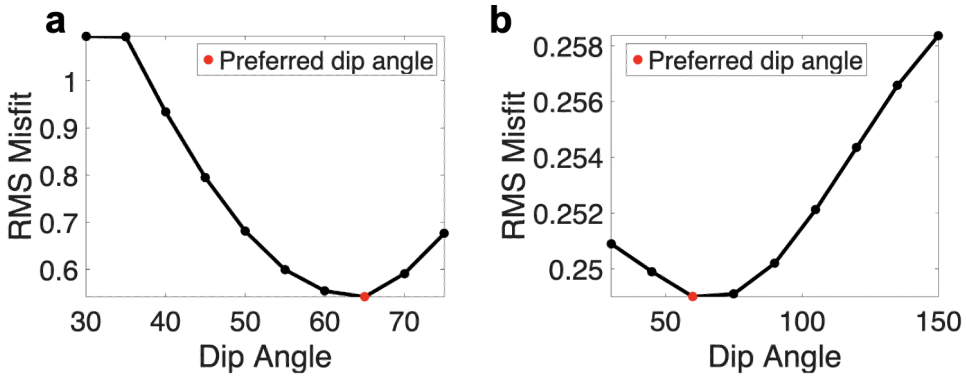

Fig. S8: The result of the initial round of dip angle grid search. Panel a: main-fault; Panel b: sub-fault. The red point represents the dip angle corresponding to the minimum RMS misfit.

Alt-text: Two-panel dip-angle grid-search results showing RMS misfit versus assumed dip angle. (a) Main-fault curve decreases from high misfit at low dip angles (30-40 degrees) to a minimum near 65 degrees, then rises again toward higher angles; a red point marks the minimum-misfit dip. (b) Sub-fault curve is U-shaped over a wider angle range (40-150 degrees) with the lowest misfit near 60 degrees (red point), and higher misfit toward both smaller and larger dip angles.

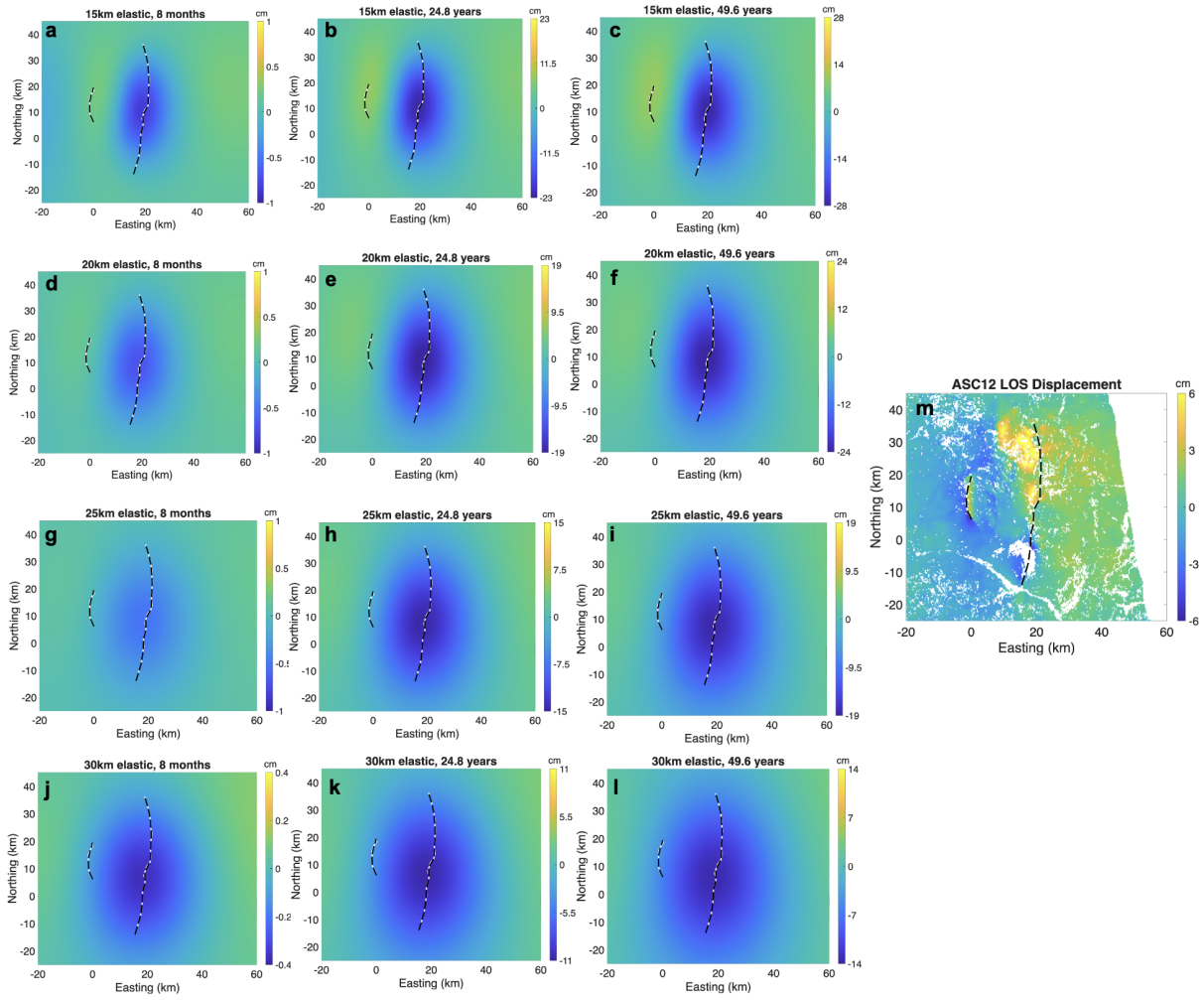

Fig. S9: The forward modeling of viscoelastic relaxation projected to the line-of-sight direction of Sentinel-1A ascending track 12. Panels a–c: 15 km elastic upper crust thickness; Panels d–f: 20 km elastic upper crust thickness; Panels g–i: 25 km elastic upper crust thickness; Panels d–f: 30 km elastic upper crust thickness. Panel m: original data. The three columns correspond to the snapshots at 8 months, half Maxwell relaxation time, full Maxwell relaxation time from left to right. The Maxwell relaxation time is calculated based on the regional rigidity and viscosity model of the upper mantle [17;18].

Alt-text: Thirteen panels of forward-modeled viscoelastic-relaxation deformation projected into Sentinel-1A ascending track 12 LOS, plus one panel of the observed LOS data. Rows a–c, d–f, g–i, and j–l show models for elastic upper-crust thicknesses of 15, 20, 25, and 30 km, respectively. Columns (left to right) are snapshots at 8 months, half Maxwell relaxation time (24.8 years), and full Maxwell relaxation time (49.6 years). Each modeled map (cm scale) shows a smooth, fault-centered LOS lobe that increases in amplitude with time; for a given time, thicker elastic crust produces smaller amplitudes. Panel m shows the original observed LOS displacement map for comparison.

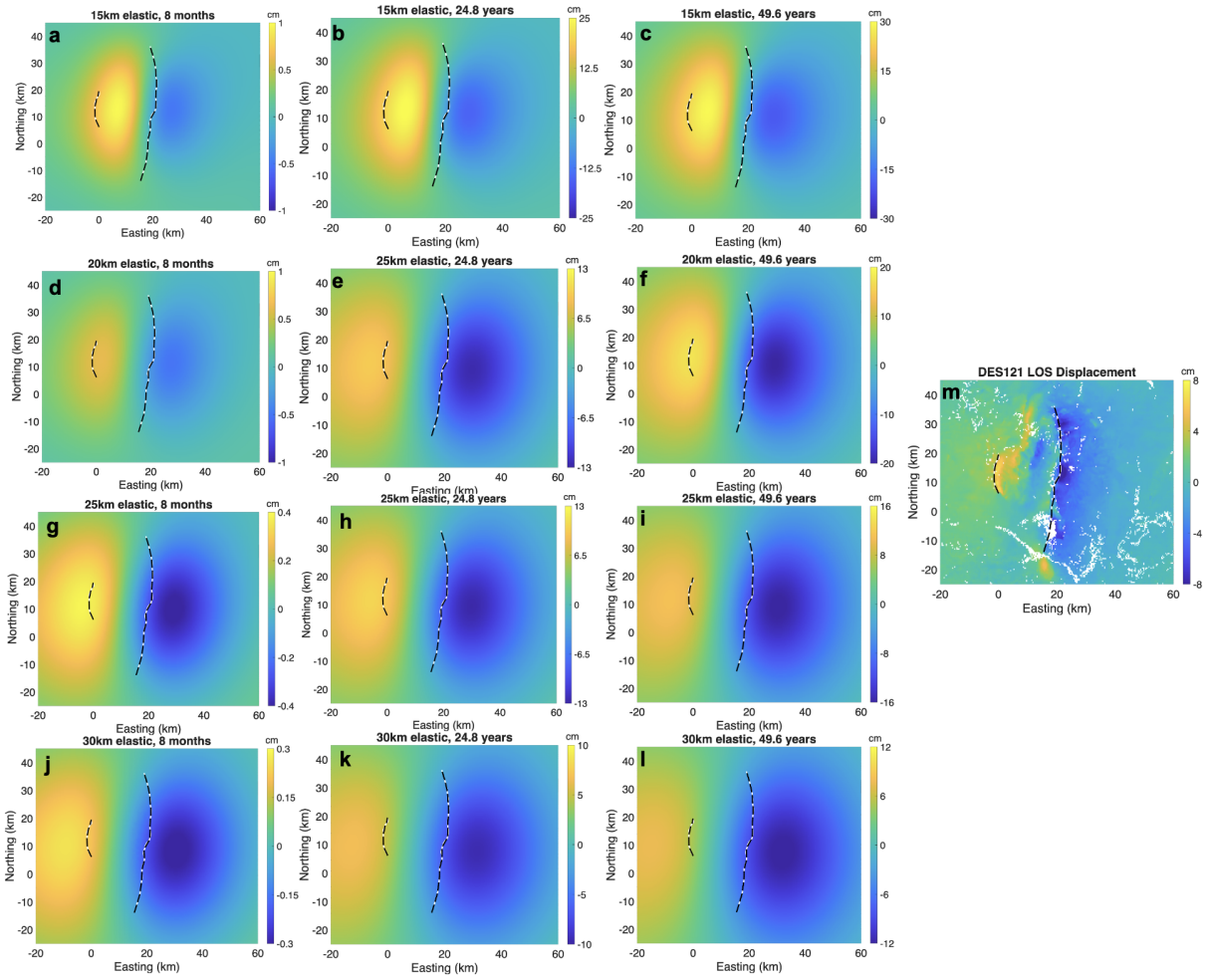

Fig. S10: The forward modeling of viscoelastic relaxation projected to the line-of-sight direction of Sentinel-1A descending track 121. Panels a–c: 15 km elastic upper crust thickness; Panels d–f: 20 km elastic upper crust thickness; Panels g–i: 25 km elastic upper crust thickness; Panels d–f: 30 km elastic upper crust thickness. Panel m: original data. The three columns correspond to the snapshots at 8 months, half Maxwell relaxation time, full Maxwell relaxation time from left to right. The Maxwell relaxation time is calculated based on the regional rigidity and viscosity model of the upper mantle [17;18].

Alt-text: Thirteen panels of forward-modeled viscoelastic-relaxation deformation projected into Sentinel-1A descending track 121 LOS, plus one panel of the observed LOS data. Rows a–c, d–f, g–i, and j–l show models for elastic upper-crust thicknesses of 15, 20, 25, and 30 km, respectively. Columns (left to right) are snapshots at 8 months, half Maxwell relaxation time (24.8 years), and full Maxwell relaxation time (49.6 years). Each modeled map (cm scale) shows a smooth, fault-centered LOS lobe that increases in amplitude with time; for a given time, thicker elastic crust produces smaller amplitudes. Panel m shows the original observed LOS displacement map for comparison.

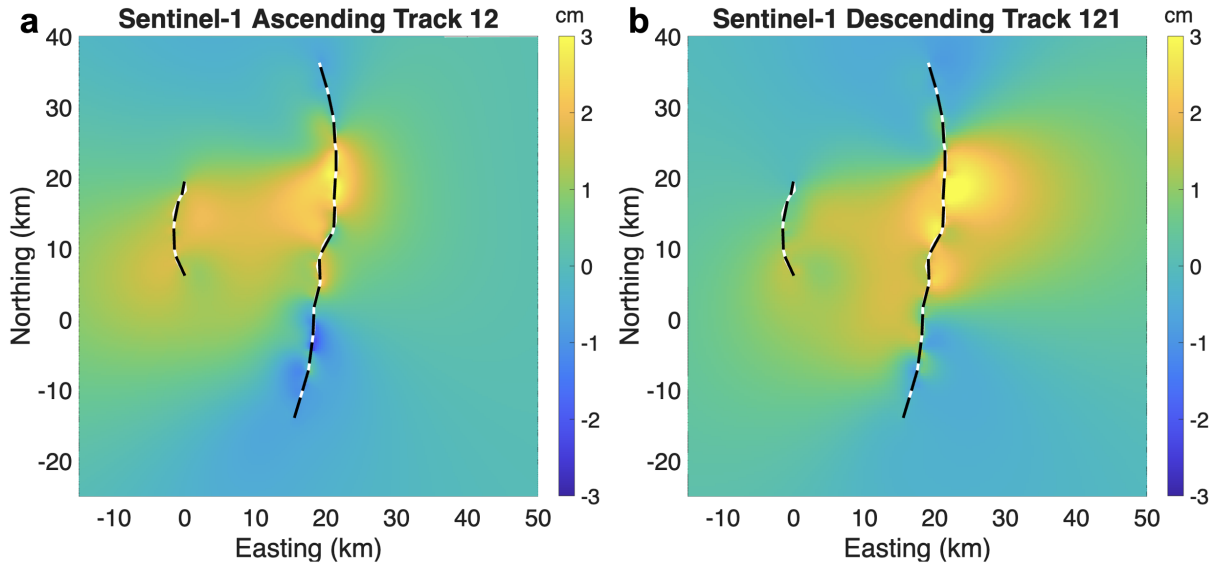

Fig. S11: The forward modeling of poroelastic relaxation projected to the line-of-sight direction of Sentinel-1A ascending track 12 (panel a) and descending track 121 (panel b). The poroelastic relaxation is computed by subtracting the coseismic displacement under the fully undrained condition (Poisson's ratio = 0.25) from that under the fully drained condition[3] (Poisson's ratio = 0.2).

Alt-text: Two maps of modeled poroelastic-relaxation LOS displacement for Sentinel-1A ascending track 12 (a) and descending track 121 (b). Both panels share the same map extent (easting and northing in km) and a color scale from -3 to 3 cm. The model shows a smooth, fault-centered pattern with a positive lobe north of the main fault trace and a negative lobe near the southern part of the fault; a smaller nearby fault segment is also plotted. Black dashed/solid lines mark the fault traces over the deformation field.

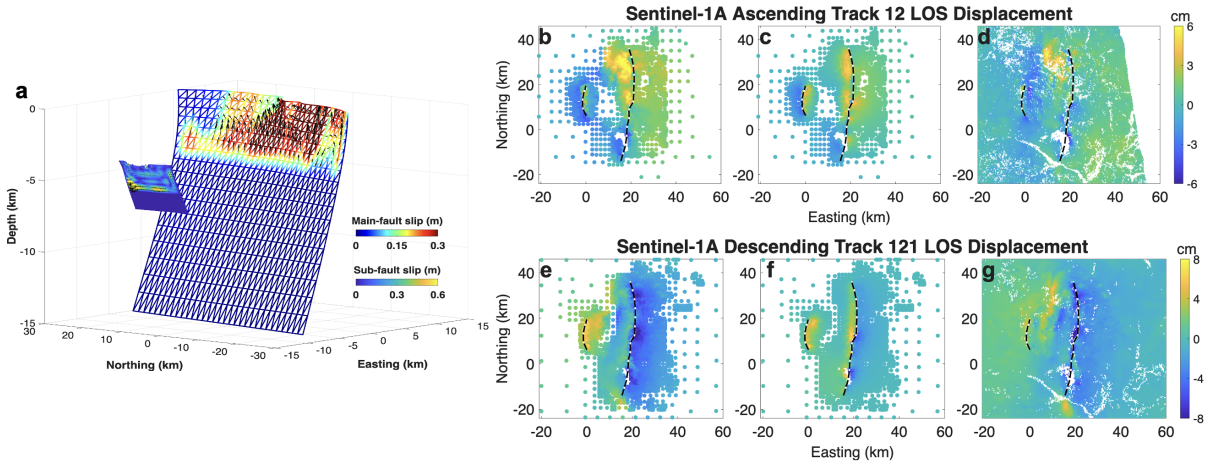

Fig. S12: Afterslip model with slip only allowed to occur in the upper 4 km depth. Panel a: slip distribution model; Panel b and e: subsampled input data; Panels c and f: forward model; Panels b and g: data-model residuals.

Alt-text: Seven-panel figure evaluating an afterslip model restricted to the upper 4 km. Panel a shows the inferred afterslip distribution on 3-D main- and sub-fault meshes (separate slip scales for each fault). For Sentinel-1A ascending track 12 (b–d) and descending track 121 (e–g), the first column shows sub-sampled LOS observations (colored points), the second column shows the forward-model LOS prediction, and the third column shows full-resolution residual maps. Color scales are in cm; residuals are generally low with localized misfit near the fault and masked areas.

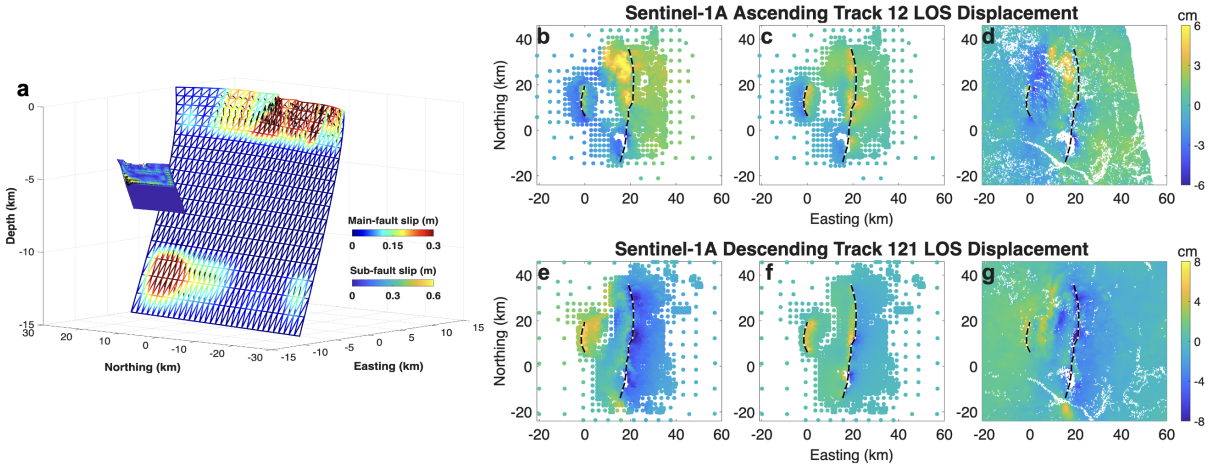

Fig. S13: Afterslip model with slip only allowed to occur in the depth lower than 3 km and greater than 11 km. Panel a: slip distribution model; Panel b and e: subsampled input data; Panels c and f: forward model; Panels b and g: data-model residuals.

Alt-text: Seven-panel figure evaluating an afterslip model with slip permitted only outside the 3–11 km depth interval. Panel a shows the inferred afterslip distribution on 3-D main- and sub-fault meshes (separate slip scales for each fault). For Sentinel-1A ascending track 12 (b–d) and descending track 121 (e–g), the first column shows sub-sampled LOS observations (colored points), the second column shows the forward-model LOS prediction, and the third column shows full-resolution residual maps. Color scales are in cm; residuals are generally low with localized misfit near the fault and masked areas.

1. References

1 Jonsson, S., Zebker, H., Segall, P. & Amelung, F. Fault slip distribution of the 1999 M_w 7.1 Hector Mine, California, earthquake, estimated from satellite radar and GPS measurements. *Bull. Seism. Soc. Am.* **92**, 1377–1389 (2002). 2

2 Simons, M., Fialko, Y. & Rivera, L. Coseismic deformation from the 1999 Mw 7.1 Hector Mine, California, earthquake as inferred from InSAR and GPS observations. *Bull. Seism. Soc. Am.* **92**, 1390–1402 (2002).

3 Jin, Z., Fialko, Y., Zubovich, A. & Schöne, T. Lithospheric deformation due to the 2015 M7.2 Sarez (Pamir) earthquake constrained by 5 years of space geodetic observations. *J. Geophys. Res.* **127**, e2021JB022461 (2022). 2, 13

4 Okada, Y. Surface deformations due to shear and tensile faults in a halfspace. *Bull. Seism. Soc. Am.* **75**, 1135–1154 (1985). 2

5 Wang, R., Martin, F. & Roth, F. Computation of deformation induced by earthquakes in a multi-layered elastic crust - FORTRAN programs EDGRN/EDCMP. *Comp. Geosci.* **29**, 195–207 (2003). 2

6 Meade, B. J. AlgorithMs for the calculation of exact displacements, strains, and stresses for triangular dislocation elements in a uniform elastic half space. *Computers & geosciences* **33**, 1064–1075 (2007). 2

7 Nikkhoo, M. & Walter, T. R. Triangular dislocation: an analytical, artefact-free solution. *Geophysical Journal International* **201**, 1119–1141 (2015). 2

8 Jin, Z., Fialko, Y., Yang, H. & Li, Y. Transient deformation excited by the 2021 M7.4 Maduo (China) earthquake: Evidence of a deep shear zone. *J. Geophys. Res.* **128**, e2023JB026643 (2023). 2

9 Fialko, Y. Probing the mechanical properties of seismically active crust with space geodesy: Study of the co-seismic deformation due to the 1992 M_w7.3 Landers (southern California) earthquake. *J. Geophys. Res.* **109**, B03307, 10.1029/2003JB002756 (2004). 2

10 Zienkiewicz, O. *The Finite Element Method* (McGraw-Hill Book Company, London, 1977), 3 edn. 2

11 Golub, G. H., Hansen, P. C. & O'Leary, D. P. Tikhonov regularization and total least squares. *SIAM journal on matrix analysis and applications* **21**, 185–194 (1999). 2

12 Meyer, M., Desbrun, M., Schröder, P. & Barr, A. H. Discrete differential-geometry operators for triangulated 2-manifolds. In *Visualization and mathematics III*, 35–57 (Springer, 2003). 2

13 Voronoi, G. Nouvelles applications des paramètres continus à la théorie des formes quadratiques. deuxième mémoire. recherches sur les parallélloèdres primitifs. *Journal für die reine und angewandte Mathematik (Crelles Journal)* **1908**, 198–287 (1908). 2

14 Devroye, L., Györfi, L., Lugosi, G. & Walk, H. On the measure of voronoi cells. *Journal of Applied Probability* **54**, 394–408 (2017). 2

15 Jin, Z. & Fialko, Y. Finite slip models of the 2019 Ridgecrest earthquake sequence constrained by space geodetic data and aftershock locations. *Bull. Seism. Soc. Am.* **110**, 1660–1679 (2020). 2

16 Jin, Z., Zou, X., Wang, K. & Fialko, Y. SlipSolve: Geodetic Linear Inversion (2025). URL https://github.com/ZeyuJin/geodetic_inversion. 2

17 Huang, S. *et al.* High-Resolution 3-D shear wave velocity model of the Tibetan Plateau: implications for custal deformation and porphyry Cu deposit formation. *Journal of Geophysical Research: Solid Earth* **125**, e2019JB019215 (2020). 11, 12

18 Tian, Z., Freymueller, J. T. & Yang, Z. Spatio-temporal variations of afterslip and viscoelastic relaxation following the Mw7.8 Gorkha (Nepal) earthquake. *Earth Planet. Sci. Lett.* **532**, 116031 (2020). 11, 12